Modeling Astrocyte-Driven Repair of Visuomotor Deficits in Alzheimer's Thalamic Circuitry

Madhuleena Dasgupta, Amit Konar, *Senior Member, IEEE*, and Atulya K. Nagar

***Abstract*—Alzheimer's Disease (AD) frequently manifests in visuomotor impairments, disrupting cholinergic signaling from the brainstem to the Thalamic Reticular Nucleus (TRN). The contribution of this work lies in the development of a biologically informed computational framework to model astrocyte mediated restoration of synaptic transmission, measured by a 'release probability (PR)' in TRN under cholinergic depletion. The model simulates three physiological states—healthy, damaged, and recovered by incorporating dual astrocytic mechanisms i.e., depolarization induced suppression excitation (DSE) and endocannabinoid mediated synaptic potentiation (e-SP). This is validated through in-vivo experiments conducted using functional near-infrared spectroscopy (fNIRS) in mice, performing visuomotor integration tasks. Both computational simulations and experimental measurements demonstrate that astrocytic feedback from functional thalamocortical relay cells (TCR) and interneurons (IN) can restore PR partially to approximately 70% of healthy levels despite complete ACh depletion. The bounded, asymmetric temporal dynamics, consistent with beta distribution characteristics reflect biologically realistic regulatory mechanisms maintaining synaptic homeostasis, exhibiting rapid initial potentiation followed by gradual decay. Sensitivity analyses reveal that when modulated with identical parameter values, excitatory TCR terminals produce greater PR with increasing astrocytic strengthening rate of indirect signaling, while inhibitory IN terminals dominate PR recovery under elevated astrocyte synapse coupling weights of indirect signaling. This highlights how excitatory and inhibitory astrocyte-targeted pathways work in tandem to shape recovery in a coordinated manner. The quantitative agreement between computational predictions and experimental measurements (within 2% error) provides evidence supporting astrocyte-based neuromodulation as a biologically grounded mechanism for restoring visuomotor function in AD.**

***Index Terms*—Alzheimer's Disease, astrocyte–neuron interaction, cholinergic depletion, synaptic recovery, thalamic circuitry**

I. INTRODUCTION

ALZEIMER'S DISEASE (AD) is a progressive neurodegenerative disorder that disrupts cognitive, sensory, and motor functions. One of the lesser addressed but functionally devastating symptoms of AD is visuomotor impairment. It impedes a patient's ability to integrate visual inputs with motor responses, thereby affecting everyday activities such as walking, navigating space, or responding to visual cues [26]. Research suggests that this impairment arises early in AD progression, making it a potential biomarker for timely diagnosis and underscoring the critical need for therapeutic interventions targeting the underlying neural circuits responsible for visuomotor integration.

The Lateral Geniculate Nucleus (LGN) serves as a central relay station in the visual pathway. It receives primary visual input from the retina and projects directly to the visual cortex. It also integrates substantial feedback from cortical areas [53]. Importantly, the LGN is one of the most densely innervated thalamic nuclei by brainstem-derived cholinergic projections, particularly Acetylcholine (ACh), the neurotransmitter responsible for cholinergic signaling [43]. Moreover, research suggests that a copy of each sensory input to thalamus is also sent to brainstem, a vital organ integrating sensory and motor pathways [48]. Thus, the role of the brainstem to thalamus pathway is the precondition for interconnecting action to perception. The above-mentioned facts implicate a vital role of the LGN (thalamus) in visuomotor deficiencies as seen in AD.

Motivated by this background, our previous work [32] developed a mathematical and computational model that captured the dynamics of the brainstem–LGN circuit under varying cholinergic conditions. That study simulated the interactions between brainstem cholinergic input and key LGN components— Thalamic Reticular Nucleus (TRN), Thalamocortical Relay Cells (TCR), and Interneurons (IN) to understand how ACh modulates thalamic oscillations, and visuomotor function. The results demonstrated that disruption in cholinergic signaling (neural communication mediated by ACh) leads to distinct bifurcation i.e., hyperpolarization in the TRN and almost no significant change in the TCR and IN outputs. Our prior work lays a foundational diagnostic framework for investigating visuomotor impairments in early-stage AD through the lens of brainstem–LGN connectivity.

The present study advances prior work [32] by moving from diagnostic modeling of visuomotor impairment towards a therapeutic framework that models intrinsic synaptic recovery. Earlier computational studies have addressed astrocyte–neuron interactions primarily in cortical and hippocampal contexts, often limited to calcium-driven signaling or amyloid-related pathology [1], [17], [49]. Other models explored gap-junctional astrocytic dynamics [33], [56] or glutamatergic processes during ischemic energy blockade [35]. However, none of these frameworks examined whether dual astrocytic pathways could support recovery of synaptic transmission under cholinergic depletion in thalamic circuits. This study addresses that gap by investigating astrocyte-mediated regulation of TRN circuitry in AD.

Astrocytes (star-shaped glial cells), once considered passive glial cells, are now recognized as active participants in synaptic

transmission. Their functions extend beyond mere support, as they are involved in synaptic regulation, blood-brain barrier maintenance, and responses to Central Nervous System (CNS) pathology [16],[55]. In [5], A. Verkhratsky introduced the "tripartite synapse" concept, highlighting astrocytic involvement in synaptic communication. Astrocytes regulate ion concentrations and neurotransmitter levels, ensuring optimal neuronal function [5]. They also form synaptic cradles, influencing synaptogenesis and synaptic plasticity [5], [16]. Inspired by these findings, our framework models astrocytic regulation of synaptic recovery in the brainstem to TRN-TCR-IN circuitry.

The Problem Statement: Visuomotor impairment in AD arises from disrupted cholinergic signaling between the brainstem and thalamic circuits. Existing computational models of AD pathology primarily focus on cortical and hippocampal circuits, leaving thalamic circuitry, particularly TRN function in visuomotor dysfunction, computationally underexplored. Current astrocyte–neuron models generally emphasize calcium-driven glutamate signaling under physiological conditions but rarely address synaptic restoration following neurotransmitter depletion. Moreover, no computational framework to date has investigated whether astrocyte-mediated synaptic pathways can compensate for the absence of ACh and partially restore synaptic transmission in brainstem to TRN–TCR–IN circuits, which are central to visuomotor integration. This gap motivates the present work, which shifts the modeling focus from ACh-dependent transmission toward astrocyte-driven regulation of the PR, aiming to uncover biologically grounded mechanisms of self-repair in thalamic circuitry. Furthermore, there is an absence of published experimental data characterizing astrocyte–TRN interactions under cholinergic depletion in AD, necessitating in-vivo validation of computational predictions. To address this dual gap, computational and empirical—the present work develops a biologically informed computational model and validates its core predictions through in-vivo experiments measuring hemodynamic responses attributed by oxygen consumption in mice performing visuomotor integration tasks under pharmacological manipulation.

Original contributions of this paper are depicted below:

1) A computational framework is developed to model astrocyte-mediated synaptic recovery in the TRN under complete cholinergic depletion, within the brainstem–LGN circuitry.
2) Dual astrocytic signaling pathways, depolarization-induced suppression of excitation (DSE) and endocannabinoid-mediated synaptic potentiation (e-SP) are integrated into a unified mathematical formulation, enabling characterization of healthy, damaged, and recovered PR.
3) The model demonstrates that indirect astrocytic signaling from functional TCR and IN terminals restores approximately 70% of healthy PR without acetylcholine reinstatement,
4) Systematic sensitivity analyses are conducted on astrocytic strengthening rates and astrocyte–synapse coupling weights, identifying distinct excitatory and inhibitory contributions to recovery dynamics.
5) Computational predictions are evaluated using in-vivo functional near infrared spectroscopy (fNIRS)-based hemodynamic measurements in mice, showing quantitative agreement (≈2% deviation) between simulated PR restoration and experimental functional preservation.

The remainder of the paper is organized as follows. Section II reviews related computational and neurobiological works relevant to cholinergic signaling, thalamic function, and astrocyte-mediated modulation. Section III includes the basic definitions required to understand the rest of the paper. Section IV describes the mathematical and computational framework that models astrocyte-mediated regulation of PR, grounded in biologically inspired mechanisms. Section V describes the computational implementation and simulation methodology, including the algorithmic framework for time-resolved analysis over 100 ms intervals. Section VI presents computational simulation experiments and results, demonstrating PR dynamics across healthy, damaged, and recovered physiological states, followed by systematic sensitivity analyses examining the influence of astrocytic strengthening rates and the effects of astrocyte–synapse coupling weight variations at TCR and IN terminals on recovery trajectories, details of which are demonstrated in Appendix A.4. Section VII provides experimental validation of the computational model through in-vivo hemodynamic measurements, demonstrating quantitative agreement between predicted PR restoration and measured neural activity preservation. Section VIII concludes by synthesizing the key findings of the paper.

II. Related Works

This section reviews prior studies that provide the biological and computational foundation for the present work, summarizing the cholinergic hypothesis of Alzheimer's Disease, outlining the role of TRN and LGN in visuomotor impairment, and presenting a comparative analysis of existing astrocyte–neuron models.

A. Cholinergic Hypothesis in Alzheimer's Disease

In [44], Francis *et al*., proposed the cholinergic hypothesis of Alzheimer's Disease (AD), stating that reduced synthesis of Acetylcholine (ACh) may have led to the disease. In [38], Steriade and McCarley suggested that neurotransmission imbalances are the possible cause of AD and consequently, the main drug-based treatment for symptomatic relief in AD is associated with the cholinergic hypothesis [38], [44]. In [4], Venkatraman *et al*. reinforced the importance of the neurotransmitter pathways in brainstem circuits. Similarly, in [51], Kar *et al*. emphasized the principal role of cholinergic depletion in AD pathology. These works together identify the cholinergic pathway from the brainstem to the thalamus as a critical domain of investigation.

B. TRN and LGN: Functional Significance in Visuomotor Impairment

According to literature, it is well known that TRN is the brain structure, which is divided into a few sections and each section

is associated with performing a different function like seeing, touching, hearing, movement etc. Each of these sections is connected to corresponding cortical area, which is associated with regulation of sensory processing and formation of rhythmic activity in thalamocortical system [8], [31]. In [53], Sherman identified the LGN as a central relay center in the visual pathway. Together, these studies highlight the importance of thalamic structures in integrating sensory information and regulating visuomotor processing.

C. Comparative Analysis with Existing Models

Earlier astrocyte–neuron computational models have focused primarily on hippocampal or cortical regions without distinguishing modulatory pathways. For example, in [49], Tewari and Majumdar proposed a tripartite synapse model, where a perisynaptic astrocyte orchestrates calcium dynamics to influence glutamate release. However, this work represented only one modulatory mechanism and modelled glutamate release as a single astrocytic pathway. In [17], Verisokin *et al*., delivered a structured model of neuron-induced calcium signaling across morphologically grounded astrocytic networks, but again limited to neuron-evoked calcium activation without explicit recovery modeling. Similarly, Pillai and Nadkarni in [1] modelled amyloid pathology in hippocampal circuits but did not incorporate astrocytic retrograde modulation beyond calcium signaling. Collectively, [1], [17], and [49] reflect calcium-driven astrocyte–neuron dynamics without distinguishing multiple pathways or recovery roles.

Beyond cortical and hippocampal contexts, additional models have examined astrocytic contributions. In [33] Goldberg *et al*., and in [56] Manninen *et al*., simulated gap-junctional astrocyte–neuron dynamics, focusing on intercellular calcium wave propagation and their role in information processing. These studies advanced understanding of calcium-based astrocytic signaling but did not address synaptic recovery under neurotransmitter depletion. Likewise, Kalia *et al*., [35] introduced a biophysically detailed glutamatergic synapse model to investigate energy blockade in ischemia, concentrating on glutamate uptake and ion transporter dynamics, processes typically mediated by astrocytes during energy failure rather than in the context of Alzheimer's-related cholinergic depletion.

In contrast, the proposed model uniquely simulates PR restoration in TRN through astrocytic feedback alone, without reinstating ACh input. It incorporates dual-modality astrocytic signaling, DSE &e-SP and explicitly examines sensitivity to astrocyte–synapse coupling strength and strengthening rates. This positions our framework as the first computational model to target TRN circuitry in AD and to capture recovery-oriented astrocytic modulation under cholinergic depletion.

III. Preliminaries

Fig.1 represents the self-repair mechanism in an astrocyte-neuron network. As demonstrated in Fig.1, a series of biological reactions take place when an action potential reaches the presynaptic terminal of a neuron. The primary function of presynaptic terminals (presynaptic axon) is to release neurotransmitters or receive glutamate (Glu) from astrocytes. The postsynaptic spine is responsible for releasing 2-arachidonylglycerol (2-AG), while the postsynaptic dendrite receives neurotransmitters. Astrocytes play a central role in connecting and converting 2-AG, inositol 1,4,5-trisphosphate (IP_3), and Glu. Moreover, these cells are crucial for facilitating self-repair. When a neuron's synapse is damaged, 2-AG, a retrograde messenger and an endocannabinoid, initiates repair mechanisms. It operates through two pathways: direct signaling i.e., depolarization-induced suppression of excitation (DSE) and indirect signaling i.e., endocannabinoid-mediated synaptic potentiation (e-SP), which work in tandem to maintain neural functionality [45].

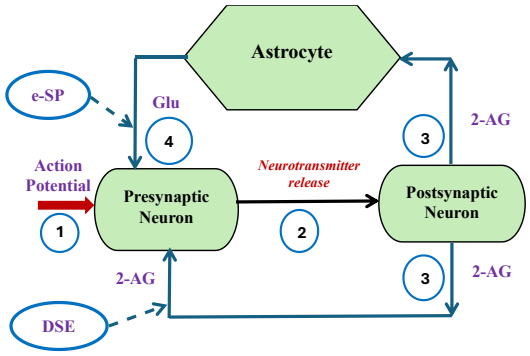

Fig.1. Astrocyte driven mechanism (1,2,3,4 represent temporal order)

Fig.2 illustrates the interplay of astrocyte-guided interactions within the brainstem-LGN circuitry, emphasizing their critical role in signal transduction under both healthy and pathological conditions. The left panel depicts the healthy state where ACh flows normally from brainstem to all LGN components (TCR, IN, TRN), enabling all three neurons to release 2-AG. In this state, 2-AG activates both direct (DSE) and indirect (e-SP) pathways. The right panel maps the recovered state following cholinergic depletion in AD, starting with restricted/depleted flow of neurotransmitter, ACh from brainstem to LGN's IN, TCR and TRN (dotted red line). Under this pathological condition, TRN loses its capacity to release 2-AG (shown by red '*X*'), eliminating both DSE and e-SP contributions from TRN itself. However, it highlights how astrocytes facilitate self-repair through the indirect signal pathway e-SP, given the presence of the retrograde messenger 2-AG from functional TCR and IN terminals. Specifically, astrocytes activated by 2-AG from surviving TCR and IN neurons release glutamate, which acts on presynaptic glutamate receptors at brainstem terminals. This e-SP mechanism increases the release probability of synaptic transmission (PR) of all the functional synapses associated with TRN, i.e., TCR and IN, and compensates for neuronal damage of TRN. This ensures functional recovery of impaired TRN circuits despite the complete absence of cholinergic input. This mechanism, referred to as astrocyte-mediated self-repair with the indirect retrograde messenger 2-AG being the key catalyst, is foundational in this study, advancing therapeutic strategies for AD. To ensure accessibility for readers across disciplines, key neurobiological terms used in this study are briefly defined

below.

Cholinergic signaling and depletion: Cholinergic signaling refers to neural communication mediated by the neurotransmitter, Acetylcholine (ACh) [43]. Cholinergic depletion denotes the reduction or loss of ACh, a condition identified as a hallmark of AD [38], [44].

Release Probability of synaptic transmission (PR): PR refers to the likelihood that a presynaptic action potential results in neurotransmitter release at the synapse. PR is regulated by both direct retrograde signaling (DSE) and astrocyte-mediated indirect signaling (e-SP).

Depolarization-induced suppression of excitation (DSE): The direct signaling pathway occurs when 2-AG binds to presynaptic cannabinoid receptors. This action inhibits the presynaptic terminal and reduces the PR of the synapse. This process is referred to as depolarization-induced suppression of excitation (DSE).

Endocannabinoid-mediated synaptic potentiation (e-SP): The indirect signaling pathway is initiated when 2-AG binds to receptors on astrocytes, causing an increase in intracellular IP_3 Once IP_3 crosses a threshold, astrocytes release glutamate, which acts on presynaptic glutamate receptors. This indirect signaling enhances PR and is termed endocannabinoid-mediated synaptic potentiation (e-SP).

Lateral Geniculate Nucleus (LGN) and its components: The LGN functions as a visual relay center that transmits retinal input to the cortex [53]. The key components of the LGN are the TRN, TCR, and IN. The TRN is subdivided into functional sectors (e.g., vision, touch, hearing, movement), each connected to a corresponding cortical area, and is involved in regulating sensory processing and generating rhythmic activity in thalamocortical circuits [8], [31], [32].

It is worth mentioning here that while TRN is exclusively GABAergic [41],[53] and is the primary source of intrathalamic inhibition [41], it exerts regulatory influence over the descending thalamocortical-ascending corticothalamic (TC–CT) glutamatergic circuits [7]. Importantly, the glutamate dynamics modelled in this study do not represent neurotransmitter release from TRN neurons themselves. Instead, glutamate here represents astrocytic gliotransmitter release acting on presynaptic terminals of brainstem cholinergic afferents through the indirect e-SP pathway [45].

This astrocyte-mediated mechanism operates as follows: The postsynaptic TRN neurons release the retrograde messenger, 2-AG, which activates the nearby astrocytes by binding to the receptors on the astrocytic processes. This binding triggers an increase in the amount of intracellular IP_3 concentration within the astrocyte. When IP_3 exceeds a threshold, glutamate is released from the astrocytes into the cytoplasm and subsequently glutamate binds to a glutamate receptor on the presynaptic terminals of brainstem cholinergic inputs, thereby enhancing PR via e-SP pathway. Thus, our model captures astrocyte-to-presynaptic signaling at brainstem terminals, not TRN-originated glutamatergic transmission.

Astrocytes: Astrocytes, once regarded as passive glial cells, are now recognized as active participants in brain function. Although non-excitable, they exhibit intracellular excitability through ion and second messenger dynamics [5], [39]. Their roles include synaptic regulation, maintaining the blood–brain barrier, modulating neurotransmitter levels, and contributing to synaptogenesis and plasticity [5], [16], [55].

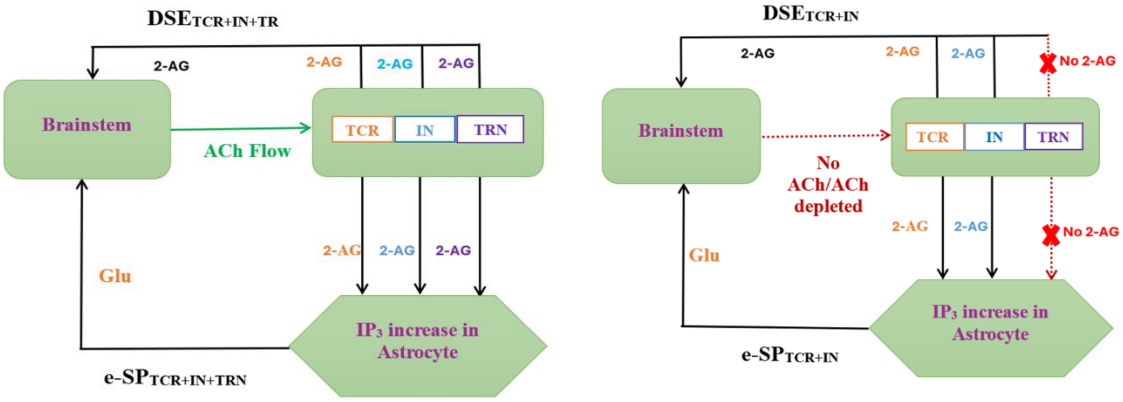

Fig. 2. Astrocyte-Guided Interactions in Brainstem-LGN Connectivity. **Left:** Healthy state with ACh flow and all components (TCR, IN, TRN) release 2-AG activating DSE and e-SP pathways. **Right:** Recovered state with ACh depleted, TRN inactive. Functional TCR and IN maintain astrocytic glutamate release to presynaptic brainstem terminals, enabling partial PR recovery of TRN via e-SP

IV. MODELING ASTROCYTE-MEDIATED SYNAPTIC DYNAMICS

Model Overview: This study develops a mathematical and simulation-based framework to investigate the restoration of PR in the TRN under pathological conditions associated with AD. The model simulates three physiological states: (1) a healthy state, (2) a damaged state marked by cholinergic loss, and (3) a recovered state in which astrocyte-mediated feedback compensates for the absence of ACh. Recovery is driven by e-SP, the indirect signaling pathway through which astrocytes modulate synaptic strength. Functional synapses from TCR and IN provide the necessary input to the TRN, facilitating compensatory modulation of PR in the absence of cholinergic signaling. This modeling framework provides a basis for understanding how astrocytic mechanisms restore visuomotor function in AD, as validated through subsequent experimental measurements.

Model Components/Simulation Setup: The model incorporates the interactions between TRN, TCR and IN in the brainstem-LGN circuitry highlighting the role of astrocytic feedback in modulating these neural connections. The core of the model involves simulating the activity of astrocytes, their feedback on synaptic transmission in brainstem-LGN circuitry, and the associated 2-AG-mediated repair mechanisms. Particularly, astrocytic feedback through DSE and e-SP are modeled as key players in synaptic modulation and self-repair in the absence of ACh. Time-series simulations are conducted to quantify PR across three physiological states: healthy, damaged, and recovered. Additionally, the sensitivity of PR recovery to varying astrocytic strengthening rates and astrocyte–synapse coupling weights are evaluated to assess the tunability of astrocytic compensation.

Rationale for Mathematical Formulation: The PR formulation follows a state-dependent linear summation framework integrating DSE and e-SP pathways under distinct physiological conditions. Detailed mathematical formulation are provided in Appendix A.1.

Astrocytic Modulation Parameters: The model incorporates two types of tunable parameters that modulate astrocytic influence on PR: (i) astrocytic strengthening rates that control how rapidly indirect signaling builds up in response to glutamate levels, and (ii) astrocyte-synapse coupling weights that determine the relative contribution of each terminal's e-SP to overall PR. These parameters are biologically motivated: strengthening rates reflect the kinetics of intracellular signaling cascades within astrocytes, while coupling weights represent the spatial and functional connectivity between astrocytic processes and different synaptic populations. In the recovered state, where TRN receives no direct ACh input, these parameters become critical for determining the extent and pattern of compensatory recovery through functional TCR and IN terminals.

The core of the model is the simulation of PR, which evolves over time in three states: healthy, damaged, and recovered. The evolution of PR is governed by separate equations for each physiological state.

$$PR_{healthy}(t) = \alpha \times DSE_{trn}(t) + \frac{1}{3}[W_{trn} \times eSP_{trn}(t) + W_{tcr} \times eSP_{tcr}(t) + W_{in} \times eSP_{in}(t)] \quad (1)$$

Equation (1) represents the PR for healthy state. 'DSE_{trn}' is the depolarization-induced suppression of excitation i.e., degree of direct signaling in TRN with a scaling factor of 'α'. '$eSP_{trn}(t)$','$eSP_{tcr}(t)$' and $eSP_{in}(t)$'represent endocannabinoid-mediated synaptic potentiation i.e., degree of indirect signaling with respect to TRN, TCR, and IN respectively. 'W_{trn}','W_{tcr}' and 'W_{in}' are the astrocyte–synapse coupling weights of indirect signaling at TRN, TCR and IN terminals respectively. The factor (1/3) in Equation (1) ensures equal weighting of the three e-SP contributions from TRN, TCR, and IN terminals. This normalization reflects the biological assumption that under healthy conditions, each neural population contributes equivalently to the baseline release probability. By scaling the combined e-SP terms by (1/3), we maintain that the total indirect signaling contribution has the same order of magnitude as the direct DSE contribution from TRN, preventing any single pathway from dominating the healthy-state PR.

$$PR_{recovered}(t) = \frac{1}{3}[W_{tcr} \times eSP_{tcr}(t) + W_{in} \times eSP_{in}(t)] \quad (2)$$

Equation (2) represents the PR for recovered state reflecting astrocytic compensation through functional TCR and IN, in the absence of direct contribution from TRN due to depletion of ACh flow in visuomotor impairment. The factor (1/3) in equation (2) normalizes the contributions from the two remaining functional terminals (TCR and IN) during recovery. In the absence of ACh, TRN no longer contributes to PR; however, we maintain proportional weighting to ensure that the combined influence of TCR and IN remains comparable to their contributions in the healthy state. This modeling choice reflects the compensatory principle that surviving synapses should collectively restore function without individual pathway dominance, thereby preserving circuit balance even under pathological conditions.

$$PR_{damaged}(t) = 0 \quad (3)$$

The damaged state is demonstrated in equation (3), indicating complete suppression of synaptic transmission due to the loss of ACh as well as absence of astrocytic input. This state represents the acute phase of neurotransmitter loss, where no recovery processes are initiated. Biologically, this corresponds to the initial impact of neuro-degeneration on the TRN circuit, where the loss of ACh disrupts synaptic function and astrocytes have not mounted a compensatory response.

Astrocyte Dynamics: The dynamics of astrocyte activation and downstream signaling are modeled using first-order differential equations. This modeling choice reflects both biological and computational rationale. Biologically, astrocytic processes follow time-dependent behaviors that often exhibit exponential decay or rise toward equilibrium. These dynamics are typically governed by rate-limited reactions and feedback mechanisms, making them well approximated by first-order kinetics. Such modeling has precedent in biophysical and neurochemical studies of astrocyte-neuron interactions [1], [23], [33]. Moreover, first-order differential equations are widely used in computational models of neuronal and glial systems, where they efficiently capture temporal integration, delay, and attenuation, all of which are central to synaptic modulation and plasticity [17]. From a computational perspective, first-order equations provide a tractable and stable framework for simulating large-scale interactions while preserving essential dynamical features. This balance makes them suitable for exploratory simulation, analysis and future implementation [13].

Astrocyte activation and its influence on synaptic signaling represent a sequential cascade of intracellular processes [45]. The sequential biochemical pathway begins with 2-AG release, followed by IP_3 production, and culminating in glutamate release. This modeling choice reflects the established biological sequence of retrograde endocannabinoid signaling:

postsynaptic 2-AG acts on presynaptic terminals and astrocytic processes. Each of these variables evolves over time in parallel for the TRN, TCR, and IN pathways. This cascade forms the basis of the model's astrocyte-mediated feedback mechanism on synaptic transmission.

$$\frac{d(AG)}{dt} = -\frac{AG}{\tau_{AG}} + \omega_{AG} \times AG \quad (4)$$

Astrocyte activation is demonstrated in equation (4). It models the temporal dynamics of 2-AG concentration. AG is the amount of 2-AG released from the postsynaptic membrane. 'τ_{AG}' represents decay rate of 2-AG, reflecting the natural degradation of 2-AG. The production rate is denoted by 'ω_{AG}' representing the rate of 2-AG synthesis from postsynaptic neurons in response to depolarization. This balance between synthesis and degradation ensures that 2-AG levels reach a steady state.

$$\frac{d(IP_3)}{dt} = -\frac{IP_3^* - IP_3}{\tau_{IP_3}} + \omega_{IP_3} \times AG \quad (5)$$

Equation (5) reflects the model of inositol 1,4,5-trisphosphate (IP_3). In this model 'IP_3' represents the concentration of inositol 1,4,5-trisphosphate within the astrocytes, while 'IP_3^*' denotes its baseline level in the context of astrocyte-mediated self-repair. When IP_3 concentration exceeds this baseline, its rate of production decreases; conversely, when IP_3 falls below the baseline, production increases. This regulation is critical for maintaining stable astrocytic function and preventing pathological fluctuations in intracellular signaling. The parameter 'τ_{IP_3}' defines the decay rate of IP_3 and 'ω_{IP_3}' represents its synthesis rate.

The relationship between IP_3 and glutamate (Glu) released from astrocytes is described by the following expression in equation (6).

$$\frac{d(Glu)}{dt} = -\frac{Glu}{\tau_{Glu}} + \omega_{Glueff} \times IP_3 \quad (6)$$

Equation (6) models glutamate release from astrocytes as a function of intracellular IP_3 concentration. The amount of glutamate released from astrocyte is indicated by 'Glu'. 'τ_{Glu}' sets the rate at which glutamate levels diminish over time, representing clearance of glutamate from the synaptic environment through multiple mechanisms including astrocytic reuptake, diffusion etc. 'ω_{Glueff}' governs the effective rate of its generation. In the simulation, to replicate the transient nature of synaptic glutamate pulses observed biologically under physiological conditions, the effective glutamate production rate was modulated over time using the following exponential decay function represented in equation (7).

$$\omega_{Glueff}(t) = \omega_{Glu} \times \exp(-t / \tau_{Geff}) \quad (7)$$

Equation (7) implements a time-dependent modulation of glutamate production to replicate the transient nature of astrocytic glutamate release. The model represents that glutamate production is strongest at the onset of astrocytic activation and declines progressively over time. 'τ_{Geff}' is the decay constant controlling the duration of glutamatergic influence. This expression reflects the biological reality that glutamate concentration at the synaptic cleft naturally declines due to vesicle depletion, astrocytic uptake, and diffusion [12], [28], [34], [40], [54].

The value of 'eSP' is influenced by the intracellular concentration of glutamate. Its temporal evolution is governed by the following differential equation (8).

$$\frac{d(eSP)}{dt} = -\frac{eSP}{\tau_{eSP}} + \omega_{eSP} \times Glu \quad (8)$$

'eSP' denotes the extent of indirect (endocannabinoid-mediated) synaptic signaling. The parameter, 'τ_{eSP}' determines the decay rate of this signal, representing the natural attenuation of potentiation over time due to multiple homeostatic processes and other regulatory mechanisms that prevent excessive potentiation. 'ω_{eSP}' reflects its amplification in response to glutamate levels. Glutamate released from astrocytes activates receptors on presynaptic terminal, leading to increased synaptic efficacy.

According to the literature [45], it is assumed that the direct signal, 'DSE' varies linearly with the quantity of 2-AG released. This relationship is captured by the expression demonstrated in equation (9):

$$DSE = \beta \times AG \quad (9)$$

'DSE' refers to the magnitude of direct signaling, and 'β_{AG}' is a negative constant, ensuring that 'DSE' remains a negative value.

Parameter Selection Rationale

Table I depicts the model parameters. The parameters are selected based on established astrocyte–neuron signaling literature [27] and tuned to ensure numerical stability and biological plausibility. Extended parameter justification and validation details are provided in Appendix A.2.

V. COMPUTER SIMULATION

Simulation Procedure: The astrocyte-mediated synaptic recovery model is implemented in Python and numerically simulated over a 100 ms time window with a uniform time-step of 0.05ms. All astrocytic and synaptic state variables are evolved using the 4th order Runge-Kutta (RK4) method. At each time-step, the biochemical dynamics of three parallel pathways: TRN, TCR, and IN are updated.

Numerical Integration Method: The differential equations governing astrocytic dynamics are integrated using the explicit RK4 method with a fixed time-step of 0.05 ms. Extended simulations confirm bounded and numerically stable PR trajectories (PR $\in$ [0,1]); the complete RK4 equations are provided in Appendix A.3.

TABLE I
MODEL PARAMETERS

Parameter	Symbol	Value	Unit
2-AG Decay	τ_{AG}	5	ms
IP_3 decay rate	τ_{IP_3}	4	ms
Glutamate decay rate	τ_{GLu}	3	ms
e-SP decay	τ_{eSP}	5	ms
2-AG production rate	ω_{AG}	0.2	μMms^{-1}
IP_3 production rate	ω_{IP_3}	0.1	μMms^{-1}
Glutamate production rate	ω_{Glu}	0.2	μMms^{-1}
IP_3 baseline	IP_3^*	1	μM
DSE scaling factor	α	0.2	dimensionless
DSE constant	β	-0.1	dimensionless
Astrocytic strengthening rate at TCR	ω_{eSPtcr}	0.15	dimensionless
Astrocytic strengthening rate at IN	ω_{eSPin}	0.15	dimensionless
Astrocytic strengthening rate at TRN	ω_{eSPtrn}	0.15	dimensionless
Astrocyte synapse coupling weight at TCR	W_{tcr}	0.4	dimensionless
Astrocyte synapse coupling weight at IN	W_{in}	0.3	dimensionless
Astrocyte synapse coupling weight at TRN	W_{trn}	0.3	dimensionless

At each simulation step: **(a)** Astrocytic states including 2-AG dynamics, intracellular IP_3 signaling, glutamate release, DSE, and e-SP are updated independently for the TRN, TCR, and IN pathways. To simulate a biologically realistic synaptic input, the glutamate production rate is modulated with an exponential decay profile, mimicking transient glutamate release shaped by vesicle depletion, diffusion, and astrocytic uptake mechanisms. **(b)** Effective synaptic input for PR computation is calculated. In the *healthy condition*, both DSE (from TRN) and e-SP (from TRN, TCR, and IN) contributed to PR. In the *recovered condition*, only e-SP from functional TCR and IN is present due to the absence of ACh input to TRN. In the *damaged condition*, PR is set to zero, reflecting total loss of synaptic transmission due to absence of ACh and astrocytic signaling. PR values are iteratively updated. In the healthy state, PR followed contributions from both direct and indirect signaling and in the recovered state, PR grow gradually under astrocytic influence alone and remained suboptimal compared to the healthy curve.

To assess model sensitivity, two classes of sensitivity analyses are conducted to explore how variation in astrocytic strengthening rates and astrocyte–synapse coupling weights at TCR and IN influence PR recovery dynamics.

PR trajectories across all simulation conditions are visualized using Python-based plotting tools to highlight condition-specific synaptic dynamics.

The proposed algorithm begins with an initialization phase of the state variables. The next step is a ***for***loop that takes care of iterating from time 0 ms to 100 ms in steps of dt = 0.05 ms using the 4th order Runge-Kutta method. Within the loop firstly effective glutamate production rate is generated, secondly, it actually performs the differential equations in an iterative manner and the response of the first, i.e., AG_{trn} is used as an input for IP_{3trn} and DSE computation. The result of IP_{3trn} is used in Glu_{trn} computation, which in turn is ultimately used in eSP_{trn}. Thirdly, the PR values are calculated for healthy, recovered and damaged states. After the ***for*** loop ends the system returns the required PR values for the whole time series.

Algorithm 1- Simulation Workflow for PR Dynamics

Inputs: Final time = 100 ms, time-step, dt = 0.05ms

Constants: $\tau_{AG}, \tau_{IP_3}, \tau_{Glu}, \tau_{eSP}, \tau_{Geff}, \omega_{AG}, \omega_{IP_3}, \omega_{Glu}, \omega_{eSP}, \alpha, \beta, IP_3^*$

Weights: W_{trn}, W_{tcr}, W_{in}

Outputs: $PR_{healthy}, PR_{recovered}, PR_{damaged}$

Begin

1. Initialize: All state variables $AG_{trn}, IP_{3trn}, Glu_{trn}, eSP_{trn}$ at time t=0 for TRN terminal. Similarly, all state variables are initiated for IN and TCR terminals.
2. ***For*** each time-step from t = 0 ms to t = 100 ms in steps of dt = 0.05ms, do:
   a. Model glutamate transient following synaptic activation:

$$\omega_{Glueff} = \omega_{Glu} * exp\left(-t/\tau_{Geff}\right)$$

   b. Update state variables at each terminal:

TRN Terminal:

$$AG_{trn} \leftarrow AG_{trn} + \left(-AG_{trn}/\tau_{AG} + \omega_{AG} \times AG_{trn}\right) * dt$$

$$IP_{3trn} \leftarrow IP3_{3trn} + \left(-\left(IP_3^* - IP_{3trn}\right)/\tau_{IP_3} + \omega_{IP_3} * AG_{trn}\right) * dt$$

$$Glu_{trn} \leftarrow Glu_{trn} + \left(-Glu_{trn}/\tau_{Glu} + \omega_{Glueff} * IP3_{trn}\right) * dt$$

$$eSP_{trn} \leftarrow eSP_{trn} + \left(-eSP_{trn}/\tau_{eSP} + \omega_{eSP} * Glu_{trn}\right) * dt$$

$$DSE_{trn} \leftarrow \beta * AG_{trn}$$

   Use similar updates with TCR and IN Terminals.

   c. Compute PR values:

$$PR_{healthy} = \alpha \times DSE_{trn} + \frac{1}{3}[W_{trn} \times eSP_{trn} + W_{tcr} \times eSP_{tcr} + W_{in} \times eSP_{in}]$$

$$PR_{recovered} = \frac{1}{3}[W_{tcr} \times eSP_{tcr} + W_{in} \times eSP_{in}]$$

$$PR_{damaged} = 0$$

End *For*

3. Print: $PR_{healthy}, PR_{recovered}, PR_{damaged}$ (each as full time-series arrays)

End

Code Availability: Upon acceptance, the complete Python implementation will be publicly available via GitHub.

VI. SIMULATION EXPERIMENTS AND RESULTS

To explore astrocyte-mediated synaptic recovery under cholinergic depletion, a series of time-resolved simulations are conducted using first-order differential equations to model the dynamic behavior of astrocytic variables across three critical synaptic terminals—TRN, TCR, and IN. Each simulation

investigates the evolution of PR in three distinct physiological states: healthy, damaged, and recovered, over a 100 ms duration with a temporal resolution of 0.05 ms using the RK4 integration method.

A. Simulation Setup

The simulation code is implemented in Python using NumPy for numerical computations and Matplotlib for visualization. All astrocytic variables—2-AG, IP_3, Glu, and e-SP are modeled as continuous-time variables governed by biologically inspired first-order differential equations. The RK4 method provides accurate numerical integration of these equations ensuring stable and physiologically realistic trajectories.

In each simulation, all variables are initialized with small non-zero values, which evolved through the following update rules: AG, IP_3 and Glu production follow exponential growth and decay dynamics. Glutamate production is modulated by a time-decaying stimulus function, mimicking natural decline due to vesicle depletion, astrocytic uptake, and diffusion. PR is computed in real-time using equations for each state: *Healthy*: Combined effect of DSE from TRN and e-SP from TRN, TCR, and IN, *Recovered:* Astrocyte-mediated e-SP from functional TCR and IN only, simulating loss of ACh. *Damaged:* Complete suppression, with PR = 0 throughout.

PR Calculation and Sensitivity Experiments: The PR is computed under three scenarios using the expressions from equations (1), (2) and (3).

To assess how different biological parameters influence recovery, additional simulations are conducted: (a) *Effect of astrocytic strengthening rate at TCR and IN*: the parameters 'ω_{eSPtcr}' and 'ω_{eSPin}', are varied individually and jointly. A 3×3 matrix of parameter combinations ranging from 0.1 to 0.3 is used to explore how the cumulative effect modulates the PR trajectory; (b) *Effect of astrocyte–synapse coupling weights at TCR and IN:* the parameters, 'W_{tcr}' and 'W_{in}' are individually varied to observe their respective contributions to PR recovery in the absence of ACh. In addition to isolated variation, a 3×3 grid of joint combinations of 'W_{tcr}' and 'W_{in}' is simulated to investigate potential synergistic or compensatory effects between excitatory and inhibitory astrocyte-synapse pathways.

B. Results

B.1. Comparative Evolution of PR: Healthy, Damaged, and Recovered Conditions

This section presents the evolution of PR in the TRN under three physiological scenarios: (1) damaged, (2) healthy, and (3) astrocyte-mediated recovery state. Fig.3 summarizes the simulated trajectories of PR in TRN under three conditions over 100 ms time frame.

In the *damaged* state (red), where there is no flow of ACh and astrocyte-neuron network is absent, PR is significantly suppressed. This reflects the synaptic dysfunction typically seen in AD, where cholinergic depletion and impaired astrocytic modulation result in diminished synaptic transmission, mimicking the patho-physiology of AD [10], [18].In the *healthy* baseline condition (green), characterized by intact cholinergic input and astrocytic regulation via both AG-mediated DSE and e-SP signaling, exhibits a rapid increase in PR, peaking at 0.126 around 21.2 ms and stabilizing into a gentle plateau. This behavior reflects robust and sustained facilitation of synaptic transmission. PR exhibited a transient asymmetric trajectory characterized by rapid initial rise, peak at 0.126 around 21.2 ms, and subsequent gradual decline. This temporal profile is consistent with beta distribution dynamics, where shape parameters α and β govern the rise and decay kinetics respectively. The condition $\alpha < \beta$ produces right-skewed profiles with steeper ascent than descent—here, the steep ascent (controlled by α) reflects fast astrocytic activation while the extended decay (controlled by β) represents slower regulatory processes. Initially, astrocyte-mediated signals synergistically elevate PR through DSE and e-SP pathways. However, over time, the system starts declining, beginning around 35 ms due to regulatory mechanisms such as receptor desensitization, gliotransmitter uptake, enzymatic degradation, and calcium store depletion [3], [9], [14], [15],[25], [36], [42], which naturally attenuate the glial response, leading to a decline after the peak. Such transient rise-and-fall dynamics is the reflection to avoid overstimulation and maintain homeostasis [29], [42]. Notably, the observed PR trajectories follow asymmetric probability distributions bounded within the physiologically valid interval [0, 1]. The temporal profile exhibits positive skewness, consistent with beta distribution characteristics where $\alpha < \beta$, characterized by steeper potentiation kinetics than decay kinetics, which resembles the transient patterns reported in earlier computational studies on astrocyte-mediated self-repair, particularly the synaptic recovery dynamics depicted in the study by [45], further supporting the biological plausibility of the modeled responses. The *recovered* condition (blue) achieves approximately 70% of healthy peak PR (recovered: 0.088; healthy: 0.126; ratio $\approx$ 0.70), through astrocytic mechanisms alone, demonstrating significant functional restoration potential in the absence of primary neurotransmitter input. This value demonstrates that: (i) substantial partial recovery (~70%) is achievable when functional TCR and IN terminals maintain astrocytic activation despite loss of TRN's own contribution and (ii) complete restoration is not achieved through astrocytic mechanisms alone, indicating inherent limitations of compensatory pathways. This computational prediction is subsequently corroborated by in-vivo experiments (Section VII), which showed 68% hemodynamic preservation under cholinergic blockade, closely matching the model's prediction with 2% deviation.

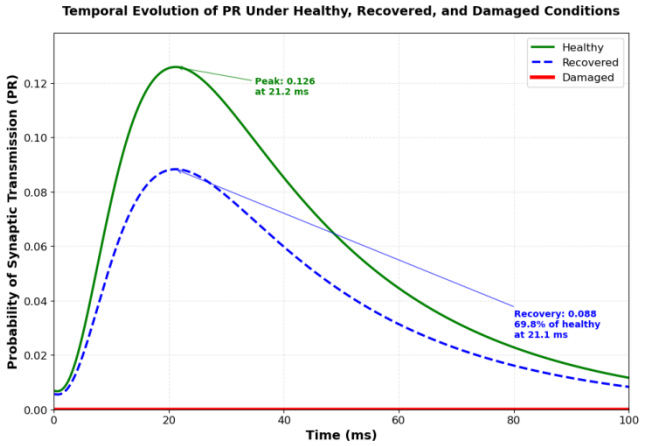

Fig.3. Comparative synaptic release probability (PR) in TRN across three simulated conditions

TABLE II
SUMMARY OF SIMULATED PR DYNAMICSUNDER CORE CONDITIONS

Condition	PR	Peak Time (ms)	Recovery Percentage	Biological Significance
Healthy	0.126	21.2	100%	Normal astrocyte-ACh synergy
Recovered	0.088	21.1	69.8%	Astrocyte-mediated compensation
Damaged	0.000	NA	0%	Complete synaptic failure

B.2 Role of astrocytic strengthening rates and astrocyte–synapse coupling weights of indirect signaling on PR recovery

Under uniform modulation of model parameters, sensitivity assessment indicates that excitatory TCR terminals exhibit greater PR enhancement with increasing astrocytic strengthening rate of indirect signaling. In contrast, inhibitory IN terminals dominate PR recovery when astrocyte–synapse coupling weights of indirect signaling are elevated. This differential response arises from the distinct parameter sensitivity of TCR and IN terminals within the indirect signaling pathway. Astrocytic strengthening rate primarily influences PR enhancement at excitatory terminals, whereas astrocyte–synapse coupling weight modulation more strongly governs recovery dynamics at inhibitory terminals. Thus, excitatory and inhibitory astrocyte-targeted indirect pathways operate in a coordinated manner and collectively shape PR restoration through parameter-dependent regulation. The detailed description of sensitivity analyses are given in Appendix A.4.

C. Stability Analysis

Stability analysis confirms that PR trajectories remain bounded within physiological limits under parameter variations. The system maintains numerical stability and convergent behavior across extended simulation intervals. No divergence, oscillatory instability, or unbounded growth is observed during indirect signaling modulation. These results validate the robustness of the recovery dynamics under astrocyte-mediated regulation. Details of stability analysis are given in Appendix A.5.

VII. IN-VIVO EXPERIMENTS TO VALIDATE SIMULATION RESULTS

To validate the model's prediction that astrocytic feedback from functional TCR and IN restores the PR in TRN to ~70% of healthy levels despite complete ACh depletion, in-vivo experiments are conducted. Hemodynamic responses attributed by oxygen consumption are measured in mice while performing a visuomotor integration task. All the experiments are conducted in AI Lab, Jadavpur University, Kolkata, satisfying the declaration of the ethics committee of Jadavpur University.

A. Experimental Framework

Thirty albino mice (aged 8–12 weeks, weighing 22.4–28.2 g) are tested using a within-subjects, repeated-measures design under three pharmacological conditions:

1. *Healthy baseline (control)*
2. *Cholinergic blockade (scopolamine)*
3. *Dual blockade (scopolamine + fluorocitrate)*

Complete data across all three conditions are obtained from N=22 mice (73.3% completion rate) following attrition across pharmacological conditions. Attrition information is provided in Appendix A.6.

Each mouse is first trained on a head-fixed go/no-go visuomotor integration task. In each trial, an auditory cue is followed by a 1-second delay, a 2-second visual stimulus (target or non-target), and a 1.5-second response window. Correct licking to the target stimulus is scored as a *Hit*, withholding licking to the non-target as *Correct Reject*, licking to non-target as *False Alarm*, and failure to lick to target as *Miss*. Training continues for 12–15 days until stable discrimination performance is achieved. The structure of the stimulus is given in Fig. 4. Experimental details are provided in Appendix A.6.

After successful training, cortical hemodynamic activity is recorded using a fNIRS system (NIRScout TM) developed by NIRx Medical Technologies, LLC) (8 sources, 8 detectors; 7.81 Hz sampling rate). Oxyhemoglobin and deoxyhemoglobin concentrations are continuously recorded.

It is worth mentioning that in the present laboratory setup, the fNIRS system achieves a maximum penetration depth of approximately 3.5 mm from the cortical surface in mice. The LGN is located at a depth of approximately 4 mm from the brain surface [18], which exceeds the penetration range of the fNIRS optodes. Consequently, hemodynamic responses attributed by oxygen consumption (*oxyhemoglobin – deoxyhemoglobin concentrations*) are recorded from the cortical area directly above the LGN. Since LGN acts as a primary thalamic relay to the cortex, thus, TRN-mediated alterations in LGN are reflected in the cortical activity [52]. The details are given in Appendix A.6.

The fNIRS recordings obtained from the scalp of each mouse capture two primary blood concentration measurements: oxyhemoglobin (O_2Hb) and deoxyhemoglobin (HHb), both measured in mmol/L. Let $\Delta O_2Hb(t)$ and $\Delta HHb(t)$ denote the concentration changes in oxyhemoglobin and deoxyhemoglobin respectively at time instant 't' during an experimental trial. Since, $\Delta O_2Hb(t) > \Delta HHb(t)$, $\forall t$, the net oxygen consumption occurring in the cortical area above the LGN region of the mouse at any time instant 't' is given by equation (10) [50].

$$C = \Delta O_2 Hb(t) - \Delta HHb(t) \quad (10)$$

Peak oxygen consumption amplitude during task performance is quantified and normalized to healthy baseline (100%) to evaluate functional preservation or collapse across conditions.

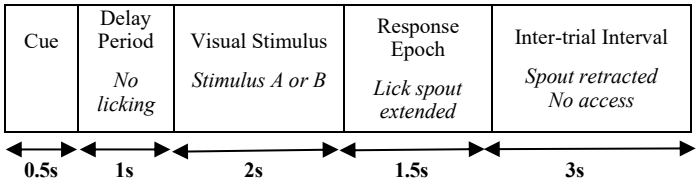

Fig.4. Structure of stimulus

B. Experimental Validation of PR restoration using Hemodynamic Analysis

The computational model predicts that astrocytic feedback can restore PR to approximately 70% during cholinergic depletion. To validate this prediction, hemodynamic responses are measured from the cortical surface in mice. It is important to note here that a direct biophysical link between PR and hemodynamic response cannot be fully established. However, the oxygen consumption measured by fNIRS reflecting neural activity serves as an indirect indicator for the functional efficacy of the LGN in brainstem-LGN circuitry. When PR is high, synaptic transmission is robust, relay neurons efficiently transmit visual information to cortex, and strong cortical activation produces large hemodynamic responses. When PR is low, synaptic transmission is impaired, relay function is compromised, and hemodynamic responses are diminished. Thus, the oxygen consumption amplitude serves as an integrated readout of circuit function, which is determined by the underlying PR values.

C. Results and Analysis for Quantitative Validation of PR Predictions

Group-level statistics reveal strong agreement between computational predictions and experimental measurements (Table III). In the healthy baseline condition, peak oxygen consumption amplitude is 2.44 ± 0.028 mmol/L (N=30), representing 100% reference activity. Under acetylcholine receptor blockade alone, hemodynamic amplitude is preserved at 1.66 ± 0.019 mmol/L (N=28, 68.0% of baseline), closely matching the model's prediction of 70% preservation with only 2.0% deviation. This preservation suggests that astrocytic compensatory mechanisms help maintain thalamocortical relay function through the LGN even when cholinergic input is blocked.

Under dual blockade, hemodynamic amplitude collapses to 0.07 ± 0.005 mmol/L (N=22, 3.0% of baseline), revealing near-complete functional loss consistent with the model's prediction of ~0% residual activity. The difference between ACh blockade alone (68.0%) and dual blockade (3.0%) is 65.0 percentage points, quantitatively isolating the astrocytic contribution to functional preservation. Since virtually all visual information reaching the cortex must first pass through the thalamus [52], the collapse of the hemodynamic response in the cortical area above the LGN under dual blockade confirms that both cholinergic and astrocytic pathways are essential for maintaining the thalamic relay/visuomotor integration tasks. The cortical hemodynamic response above LGN region is demonstrated in Fig.5.

TABLE III
GROUP HEMODYNAMIC RESPONSES ACROSS EXPERIMENTAL CONDITIONS

Condition	N	Mean Oxygen consumption (mmol/L)	SD (mmol/L)	SEM (mmol/L)	% of Healthy
Healthy Baseline	30	2.44	0.155	0.028	100
ACh Blockade	28	1.66	0.103	0.019	68
Dual Blockade	22	0.07	0.022	0.005	3

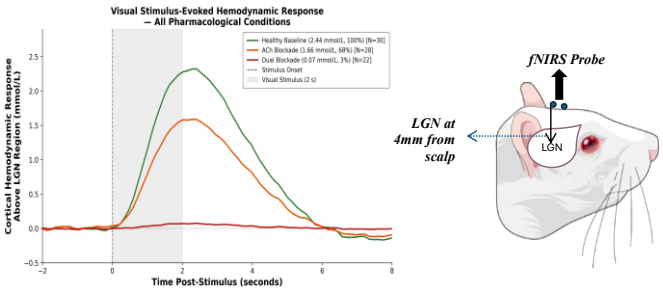

Fig. 5. Cortical Hemodynamic Response above LGN region

VIII. CONCLUSION

This study presents a computational–experimental framework demonstrating astrocyte-mediated restoration of PR of the TRN under cholinergic depletion in AD. We develop a biophysically grounded model incorporating dual astrocytic signalling mechanisms and simulate three synaptic states: healthy, cholinergic depletion, and dual blockade (cholinergic depletion with astrocytic inhibition). The model predicts that, despite complete ACh loss, astrocytic feedback preserves approximately 70% of healthy output.

In-vivo experiments using a sequential pharmacological blockade paradigm combined with fNIRS-based hemodynamic measurements during a visuomotor integration task yield results consistent with this prediction. Cholinergic blockade alone preserves ~68% of baseline healthy condition, whereas dual blockade (cholinergic and astrocytic inhibition) results in near-complete collapse (~3%), quantitatively isolating the astrocytic contribution. The close agreement between simulated and experimental outcomes supports the proposed mechanism of astrocyte-mediated synaptic stabilization in thalamocortical circuits.

Therapeutically, these findings shift emphasis from purely neurotransmitter replacement strategies toward astrocyte-mediated compensation. Targeting astrocyte–neuron interactions may provide a complementary strategy to mitigate visuomotor dysfunction in AD.

A limitation of this study is that the experimental validation relies on hemodynamic measurements obtained using fNIRS. These signals reflect neurovascular responses associated with neural activity rather than direct measurements of PR. Furthermore, these signals encompass multiple biological processes including neuronal firing rate, excitatory–inhibitory balance, astrocytic metabolic activity, and vascular coupling. Therefore, the observed preservation of oxygen consumption provides indirect functional evidence consistent with the

modeled PR restoration but does not directly confirm the model's quantitative prediction of synaptic recovery. Future work will incorporate electrophysiological recordings or calcium imaging to provide more direct validation of astrocyte-mediated synaptic dynamics in thalamic circuitry.

REFERENCES

[1] A. G. Pillai and S. Nadkarni, "Amyloid pathology disrupts gliotransmitter release in astrocytes," PLoSComput. Biol., vol. 18, no. 8, Art. no. e1010334, Aug. 2022, doi: 10.1371/journal.pcbi.1010334.

[2] A. Panatier et al., "Glia-derived D-serine controls NMDA receptor activity and synaptic memory," Cell, vol. 125, no. 4, pp. 775–784, May 2006, doi: 10.1016/j.cell.2006.02.051.

[3] A. Raveh, R. Turecek, and B. Bettler, "Mechanisms of fast desensitization of GABA(B) receptor-gated currents," Adv. Pharmacol., vol. 73, pp. 145–165, 2015, doi: 10.1016/bs.apha.2014.11.004.

[4] A. Venkatraman, B. L. Edlow, and M. H. Immordino-Yang, "The brainstem in emotion: A review," Front. Neuroanat., vol. 11, Art. no. 15, Feb. 2017, doi: 10.3389/fnana.2017.00015.

[5] A. Verkhratsky, "Astrocytes," in Oxford Research Encyclopedia of Neuroscience. Oxford, U.K.: Oxford Univ. Press, 2024, doi: 10.1093/acrefore/9780190264086.013.516.

[6] A. Yu and A. Y. Lau, "Glutamate and glycine binding to the NMDA receptor," Structure, vol. 26, no. 7, pp. 1035–1043.e2, Jul. 2018, doi: 10.1016/j.str.2018.05.004.

[7] B. P. Nabit, A. Taylor, and D. G. Winder, "Thalamocortical mGlu8 modulates dorsal thalamus excitatory transmission and sensorimotor activity," J. Neurosci., vol. 44, no. 31, Art. no. e0119242024, Aug. 2024, doi: 10.1523/JNEUROSCI.0119-24.2024.

[8] B. S. Bhattacharya, T. P. Bond, L. O'Hare, D. Turner, and S. J. Durrant, "Causal role of thalamic interneurons in brain state transitions: A study using a neural mass model implementing synaptic kinetics," Front. Comput. Neurosci., vol. 10, Art. no. 115, Nov. 2016, doi: 10.3389/fncom.2016.00115.

[9] C. Agulhon et al., "Calcium signaling and gliotransmission in normal vs. reactive astrocytes," Front. Pharmacol., vol. 3, Art. no. 139, Jul. 2012, doi: 10.3389/fphar.2012.00139.

[10] C. Henneberger, T. Papouin, S. H. Oliet, and D. A. Rusakov, "Long-term potentiation depends on release of D-serine from astrocytes," Nature, vol. 463, no. 7278, pp. 232–236, Jan. 2010, doi: 10.1038/nature08673.

[11] C. Nanclares, A. M. Baraibar, A. Araque, and P. Kofuji, "Dysregulation of astrocyte-neuronal communication in Alzheimer's disease," Int. J. Mol. Sci., vol. 22, no. 15, Art. no. 7887, Jul. 2021, doi: 10.3390/ijms22157887.

[12] D. E. Bergles and J. D. Rothstein, "Glutamate uptake by astroglia," in Neuroglia. Boston, MA, USA: Springer, 2004, pp. 239–261, doi: 10.1007/978-1-4020-7937-5_9.

[13] D. Reato et al., "Computational model of neuron-astrocyte interactions during focal seizure generation," Front. Comput. Neurosci., vol. 6, Art. no. 81, Oct. 2012, doi: 10.3389/fncom.2012.00081.

[14] E. A. Newman and A. Volterra, "Glial control of synaptic function," Glia, vol. 47, no. 3, pp. 207–208, Aug. 2004, doi: 10.1002/glia.20085.

[15] E. Grady *et al*., "Mechanisms attenuating cellular responses to neuropeptides: extracellular degradation of ligands and desensitization of receptors," J. Investig. Dermatol. Symp. Proc., vol. 2, no. 1, pp. 69–75, 1997, doi: 10.1038/jidsymp.1997.14.

[16] E. M. Hol, E. A. van Vliet, and E. Aronica, "Astrocyte functions in health and disease," in Handbook of Clinical Neurology, vol. 165. Amsterdam, Netherlands: Elsevier, 2024, pp. 43–65, doi: 10.1201/9781003389699-3.

[17] E. M. Vrisokin, D. V. Verveyko, D. E. Postnov, and A. R. Brazhe, "Modeling of astrocyte networks: Toward realistic topology and dynamics," Front. Cell. Neurosci., vol. 15, Art. no. 645068, Jun. 2021, doi: 10.3389/fncel.2021.645068.

[18] E. Mounier, B. Abdullah, H. Mahdi, and S. Eldawlatly, "A deep convolutional visual encoding model of neuronal responses in the LGN," *Brain Informatics*, vol. 8, no. 1, p. 11, 2021, doi: 10.1186/s40708-021-00132-6.

[19] G. Perea et al., "Activity-dependent switch of GABAergic inhibition into glutamatergic excitation in astroyte-neuron networks," eLife, vol 5, Art. no. e20362, Dec.2016, doi: 10.7554/eLife.20362.

[20] H. Kawano et al., "Astrocytes with previous chronic exposure to amyloid β-peptide fragment 1-40 suppress excitatory synaptic transmission," J. Neurochem., vol. 143, no. 6, pp. 624–634, Dec. 2017, doi: 10.1111/jnc.14247.

[21] H. Zhuang, D. Yuan, F. Shi, X. Wu, Z. Luo, and W. Gan, "The dose-dependent effects of fluorocitrate on the metabolism and activity of astrocytes and neurons," *Brain Sciences*, vol. 15, no. 2, p. 99, Jan. 2025, doi: 10.3390/brainsci15020099.

[22] I. Klinkenberg and A. Blokland, "The validity of scopolamine as a pharmacological model for cognitive impairment: A review of animal behavioral studies," *Neuroscience and Biobehavioral Reviews*, vol. 34, no. 8, pp. 1307–1350, Jul. 2010, doi: 10.1016/j.neubiorev.2010.04.001.

[23] J. J. Wade, L. J. McDaid, J. Harkin, V. Crunelli, and J. A. Kelso, "Bidirectional coupling between astrocytes and neurons mediates learning and dynamic coordination in the brain: A multiple modeling approach," PLoS One, vol. 6, no. 12, Art. no. e29445, Dec. 2011, doi: 10.1371/journal.pone.0029445.

[24] J. Koeppen et al., "Functional consequences of synapse remodeling following astrocyte-specific regulation of ephrin-B1 in the adult hippocampus," J. Neurosci., vol. 38, no. 25, pp. 5710–5726, Jun. 2018, doi: 10.1523/JNEUROSCI.0618-18.2018.

[25] J. Riquelme, M. Wellmann, R. Sotomayor-Zárate, and C. Bonansco, "Gliotransmission: A novel target for the development of antiseizure drugs," Neuroscientist, vol. 26, no. 4, pp. 293–309, Aug. 2020, doi: 10.1177/1073858420901474.

[26] J. Staal, F. U. S. Mattace-Raso, H. Daniels, J. van der Steen, and J. J. M. Pel, "To explore the predictive power of visuomotor network dysfunctions in mild cognitive impairment and Alzheimer's disease," Front. Neurosci., vol. 15, Art. no. 654003, Apr. 2021, doi: 10.3389/fnins.2021.654003.

[27] J. Wade, L. McDaid, J. Harkin, V. Crunelli, and S. Kelso, "Self-repair in a bidirectionally coupled astrocyte-neuron (AN) system based on retrograde signaling," *Frontiers in Computational Neuroscience*, vol. 6, p. 76, Sep. 2012, doi: 10.3389/fncom.2012.00076.

[28] J.-P. Kessler, "Control of cleft glutamate concentration and glutamate spill-out by perisynaptic glia: Uptake and diffusion barriers," PLoS One, vol. 8, no. 8, Art. no. e70791, Aug. 2013, doi: 10.1371/journal.pone.0070791.

[29] K. T. Baldwin, K. K. Murai, and B. S. Khakh, "Astrocyte morphology," Trends Cell Biol., vol. 34, no. 7, pp. 547–565, Jul. 2024, doi: 10.1016/j.tcb.2023.09.006.

[30] K. Takuma, A. Baba, and T. Matsuda, "Astrocyte apoptosis: implications for neuroprotection," Prog. Neurobiol., vol. 72, no. 2, pp. 111–127, Feb. 2004, doi: 10.1016/j.pneurobio.2004.02.001.

[31] M. Beierlein, "Synaptic mechanisms underlying cholinergic control of thalamic reticular nucleus neurons," J. Physiol., vol. 592, no. 19, pp. 4137–4145, Oct. 2014, doi: 10.1113/jphysiol.2014.274274.

[32] M. Dasgupta, B. S. Bhattacharya, and A. K. Nagar, "Linking brainstem cholinergic input to thalamocortical circuitry," in Proc. Soft Comput. Problem Solving, vol. 1. New Delhi, India: Springer, 2017, pp. 375–386.

[33] M. Goldberg, M. De Pittà, V. Volman, H. Berry, and E. Ben-Jacob, "Nonlinear gap junctions enable longdistance propagation of pulsating calcium waves in astrocyte networks," PLoSComput. Biol., vol. 6, no. 8, Art. no. e1000909, Aug. 2010, doi: 10.1371/journal.pcbi.1000909

[34] M. I. Glavinović, "Monte carlo simulation of vesicular release, spatiotemporal distribution of glutamate in synaptic cleft and generation of postsynaptic currents," Pflugers Arch. Eur. J. Physiol., vol. 437, no. 3, pp. 462470, Feb. 1999, doi: 0.1007/s004240050802.

[35] M. Kalia, H. G. E. Meijer, S. A. van Gils, M. J. A. M. van Putten, and C. R. Rose, "Ion dynamics at the energy-deprived tripartite synapse," PLoSComput. Biol., vol. 17, no. 6, Art. no. e1009019, Jun. 2021, doi: 10.1371/journal.pcbi.1009019.

[36] M. Rangel-Gomez et al., "Neuron-glial interactions: Implications for plasticity, behavior, and cognition," J. Neurosci., vol. 44, no. 40, Art. no. e1231242024, Oct. 2024 doi: 10.1523/JNEUROSCI.1231-24.2024.

[37] M. Saponati, J. Garcia-Ojalvo, E. Cataldo, and A. Mazzoni, "Thalamocortical spectral transmission relies on balanced input strengths," Brain Topogr., vol. 35, no. 1, pp. 4–18, Jan. 2022, doi: 10.1007/s10548-02100851-3.
[38] M. Steriade and R. W. McCarley, Brain Control of Wakefulness and Sleep, 2nd ed. New York, NY, USA: Springer, 2005.
[39] M. V. de O. Santana et al., "Study of the characteristics and functions of astrocytes of the nervous system," Middle East Res. J. Med. Sci., vol. 4, no. 5, pp. 135–148, Sep.–Oct. 2024.
[40] N. C. Danbolt, "Glutamate uptake," Prog. Neurobiol., vol. 65, no. 1, pp. 1–105, Sep. 2001, doi: 10.1016/s0301-0082(00)00067-8.
[41] N. Hádinger, K. Bölcskei, E. S. Vizi, Z. Szabó, M. L. Lőrincz, A. Tóth, and B. Sperlágh, " Region-selective control of the thalamic reticular nucleus via cortical layer 5 pyramidal cells", *Nat Neurosci* **26**, 116–130 (2023). https://doi.org/10.1038/s41593-022-01217-z
[42] N. Vardjan and R. Zorec, "Excitable astrocytes: Ca(2+)- and cAMP-regulated exocytosis," Neurochem.Res., vol. 40, no. 12, pp. 2414–2424, Dec. 2015, doi: 10.1007/s11064-015-1545-x.
Nov. 2004.
[43] P. Kasa, Z. Rakonczay, and K. Gulya, "The cholinergic system in Alzheimer's disease," Prog. Neurobiol., vol. 52, no. 6, pp. 511–535, Aug. 1997, doi: 10.1016/S0301-0082(97)00028-2.
[44] P. T. Francis, A. M. Palmer, M. Snape, and G. K. Wilcock, "The cholinergic hypothesis of Alzheimer's disease: a review of progress," J. Neurol. Neurosurg. Psychiatry, vol. 66, no. 2, pp. 137–147, Feb. 1999, doi: 10.1136/jnnp.66.2.137.
[45] Q. Hong, H. Chen, J. Sun, and C. Wang, "Memristive circuit implementation of a self-repairing network based on biological astrocytes in robot application," IEEE Trans. Neural Netw. Learn. Syst., vol. 33, no. 5, pp. 2106–2120, May 2022, doi: 10.1109/TNNLS.2020.3041624.
[46] R. A. Chiareli et al., "The role of astrocytes in the neurorepair process," Front. Cell Dev. Biol., vol. 9, Art. no. 665795, May 2021, doi: 10.3389/fcell.2021.665795.
[47] R. Siracusa, R. Fusco, and S. Cuzzocrea, "Astrocytes: Role and functions in brain pathologies," Front. Pharmacol., vol. 10, Art. no. 1114, Sep. 2019, doi: 10.3389/fphar.2019.01114.
[48] R. W. Guillery, "Branching thalamic afferents link action and perception," J. Neurophysiol., vol. 90, no. 2, pp. 539–548, Aug. 2003, doi: 10.1152/jn.00337.2003.
[49] S. G. Tewari and K. K. Majumdar, "A mathematical model of the tripartite synapse: astrocyte-induced synaptic plasticity," J. Biol. Phys., vol. 38, no. 3, pp. 465–496, Jun. 2012, doi: 10.1007/s10867-012-9267-7.
[50] S. Ghosh, A. Konar, and A. K. Nagar, "Assessment of scientific creative-potential by near-infrared spectroscopy using brain-network-based deep-fuzzy classifier," *IEEE Access*, vol. 13, pp. 108533–108550, 2025
[51] S. Kar, P. M. Slowinski, D. Westaway, and H. T. J. Mount, "Interactions between β-amyloid and central cholinergic neurons: implications for Alzheimer's disease," J. Psychiatry Neurosci., vol. 29, no. 6, pp. 427–441,
[52] S. M. Sherman and R. W. Guillery, "The role of the thalamus in the flow of information to the cortex," Philos. Trans. R. Soc. London, Ser. B, vol. 357, no. 1428, pp. 1695–1708, Dec. 2002, doi: 10.1098/rstb.2002.1161.
[53] S. M. Sherman, "Thalamus," Scholarpedia, vol. 1, no. 9, Art. no. 1583, 2006. doi:10.4249/scholarpedia.1583
[54] S. Makani and E. Zagha, "Out of the cleft: the source and target of extra-synaptic glutamate in the CA1 region of the hippocampus," J. Physiol., vol. 582, no. 2, pp. 479–480, Jul. 2007, doi: 10.1113/jphysiol.2007.137059.
[55] T. M. Fisher and S. A. Liddelow, "Emerging roles of astrocytes as immune effectors in the central nervous system," Trends Immunol., vol. 45, no. 10, pp. 824–836, Oct. 2024, doi: 10.1016/j.it.2024.08.008.
[56] T. Manninen, R. Havela, and M. L. Linne, "Computational models for calcium-mediated astrocyte functions," Front. Comput. Neurosci., vol. 12, Art. no. 14, Feb. 2018, doi: 10.3389/fncom.2018.00014.

MADHULEENA DASGUPTA received the comprehensive M.Sc. degree in micro and nano systems from Technische Universität Chemnitz, Germany, and the Ph.D. degree in Computer Science (Health Informatics) from Liverpool Hope University, U.K., where she was awarded the Vice-Chancellor's Scholarship. She is currently a Research Fellow with Liverpool Hope University, UK within the School of Computer Science and the Environment. Her research lies at the intersection of computational neuroscience and mathematical modelling of neural systems, with a focus on neural circuit dynamics and neurotransmitter-mediated processes underlying cognition. Her work further extends to the modelling of astrocyte–neuron networks, aiming to develop biologically grounded frameworks for therapeutic strategies in neurological and neurodegenerative disorders. She is a recipient of the Best Paper Award at the International Conference on Soft Computing for Problem Solving (SocProS), 2017, and has extensive experience in interdisciplinary research, collaborating with international academic and research institutions.

AMIT KONAR (SM' 2010) is currently a Professor in the department of Electronics and Tele-Communication Engineering, Jadavpur University, Kolkata, India. He earned his B.E. degree in Electronics and Tele-Communication Engineering from Indian Institute of Engineering Science and Technology (previously, Bengal Engineering College), Kolkata in 1983, his M.E. degree in Control Engineering, M. Phil. degree in System Modelling and Ph.D. degree in Artificial Intelligence, all from Jadavpur University in 1985, 1988 and 1994 respectively.

Dr. Konar is the author of 15 books including two popular texts, Artificial Intelligence and Soft Computing: Behavioral and Cognitive Modeling of the Human Brain, (CRC Press) in 2000 and Computational Intelligence: Principles, Techniques and Applications, (Springer) in 2005. He has published 35 peer-reviewed book chapters and over 100 research papers in leading international journals (including 29 IEEE Transactions), and over 250 research papers published in IEEE Flagship Conference proceeedings. He has supervised 29 Ph.D. theses and over 400 Masters theses, all in the broad area of Cognitive Neuro-science, AI and Robotics. Dr. Konar delivered keynote/tutorial speech in top flagship IEEE Conferences including WCCI-2020 and ICASSP-2016. He has been serving as the Associate Editor of IEEE TFS and IEEE TETCI for several years. Dr. Konar is currently the EIC of the Springer book series on Cognitive Intelligence and Robotics. He served as the Coordinator/Principal Investigator of several National level projects funded by Government of india and industries. His current research interest includes Cognitive Neuroscience, Type-2 Fuzzy Logic, Multi-agent Systems and Scientific Creativity.

ATULYA K. NAGAR is Foundation Chair and Professor of Mathematical Sciences and Pro Vice-Chancellor (Research) at Liverpool Hope University (LHU), UK. He leads the University's research strategy and development of science and engineering, having previously served as Founding Dean of the Faculty of Science and inaugural Head of the School of Mathematics, Computer Science and Engineering, which he established. He received B.Sc. (Hons.), M.Sc., and M.Phil. (Hons.) degrees in Mathematical Physics from MDS University of Ajmer, India, and was awarded a prestigious Commonwealth Fellowship to pursue a D.Phil. in Applied Nonlinear Mathematics at the University of York, UK (1996). Prior to joining LHU in 2001, he held academic positions at the University of York, Brunel University London, and other institutions. An internationally recognised scholar, his research spans nonlinear mathematics, theoretical computer science, and computational methods with applications in science and engineering. He has authored over 550 publications and edited several volumes in applied mathematics and intelligent systems, and co-edits Springer book series in these areas. Professor Nagar holds visiting professorships at leading institutions in India, including IIT Roorkee, South Asian University, and the University of Madras, where he was appointed Sir C. V. Raman Chair, funded by the Nobel Laureate Sir C. V. Raman Endowment. He has served as an expert reviewer for UKRI councils including EPSRC, BBSRC, and AHRC, and contributes to national research policy through roles such as the JISC Research Strategy Group, UKRI Talent Panel College, and REF 2029 PCE Pilot Panel. He is a Fellow of the Institute of Mathematics and its Applications (FIMA) and the Higher Education Academy (FHEA).

Appendix

A.1 *Rationale for Mathematical Formulation*

Linear Additivity Assumption: Release probability of synaptic transmission (PR) is influenced by multiple concurrent modulatory signals. In the absence of detailed biophysical data on nonlinear interactions between depolarization-induced suppression of excitation (DSE) and endocannabinoid-mediated synaptic potentiation (e-SP) pathways, a linear summation model is adopted. This approach has been successfully employed in memristive circuit implementations of biological astrocyte-neuron networks, where PR is modelled as the weighted sum of direct (DSE) and indirect (e-SP) signaling pathways [45].

State-Dependent Formulation: The three PR equations (healthy, recovered, damaged) reflect distinct pathophysiological scenarios. The healthy state incorporates all available modulatory pathways including direct Acetylcholine (ACh)-dependent signaling via DSE; the recovered state excludes thalamic reticular nucleus's (TRN) own DSE and e-SP contributions due to ACh depletion but retains compensatory mechanisms from surviving TCR and IN terminals; and the damaged state represents complete circuit failure in the absence of both neurotransmitter input and astrocytic support.

A.2 *Parameter Selection Rationale*

Model parameters are selected based on general timescales reported in astrocyte-neuron signaling literature [27] and tuned to ensure: (1) numerical stability with bounded probability values (PR ∈ [0,1]), (2) biologically plausible temporal dynamics characterized by rapid potentiation followed by gradual decay, and (3) quantitative agreement with experimental validation. Due to the absence of published experimental data characterizing astrocyte-TRN interactions under cholinergic depletion in brainstem-LGN circuitry, the computational model is validated through in-vivo experiments. The model predicted ~70% PR restoration under cholinergic blockade, which is experimentally confirmed with 68% neural activity preservation (N=28), demonstrating only 2% deviation between computational prediction and experimental measurement. Dual blockade experiments (cholinergic plus astrocytic inhibition, N=22) causally confirmed that the preserved activity under ACh blockade alone is specifically attributable to astrocytic compensation, with activity collapsing to 3% when both systems are impaired. This quantitative agreement between computational predictions and biological measurements supports both the parameter selection and the underlying astrocyte-mediated recovery mechanism for brainstem-LGN circuitry.

Numerical validation: All parameter combinations maintain numerical stability with 4th order Runge-Kutta method (dt = 0.05 ms). Extended 200 ms simulations confirm stable, bounded trajectories (PR ∈ [0,1]) without numerical instabilities.

A.3 *Numerical Integration Method*

Numerical Integration Method: The differential equations governing astrocytic dynamics are integrated using the explicit 4th order Runge-Kutta (RK4) method with a fixed time step of 0.05 ms. RK4 is selected for several key reasons firstly, higher-order accuracy enabling accurate capture of astrocytic dynamics with coarser time steps; secondly, stability: simulations extended to 200 ms confirm stable, bounded PR trajectories (PR ∈ [0,1]) without numerical drift or instability, validating the method's appropriateness for this system and thirdly, simplicity. The RK4 update procedure for each state variable 'y' follows:

$$k_1 = f(t_n, y_n)$$

$$k_2 = f(t_n + \frac{1}{2}h, y_n + \frac{1}{2}k_1 h)$$

$$k_3 = f(t_n + \frac{1}{2}h, y_n + \frac{1}{2}k_2 h)$$

$$k_4 = f(t_n + h, y_n + k_3 h)$$

$$y_{n+1} = y_n + \frac{h}{6}[k_1 + 2k_2 + 2k_3 + k_4]$$

where, 'f'' is determined from the governing equations for AG, IP_3, Glu, and e-SP at each terminal (TCR, TRN, IN).

A.4 Sensitivity Analysis

Role of astrocytic strengthening rates of indirect signaling on PR recovery

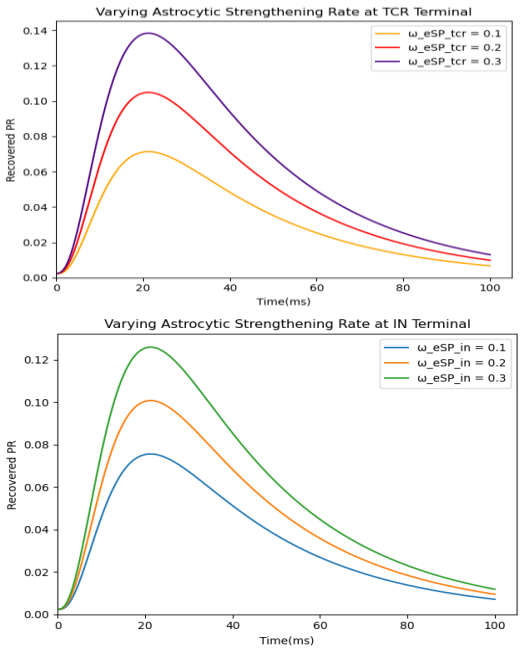

Fig.1. Recovery dynamics of TRN by varying strengthening rate of indirect signaling at TCR terminal (top) and IN terminal (bottom)

In Fig. 1, increasing the astrocytic strengthening rate of indirect signaling at TCR, 'ω_{eSPtcr}' produces higher PR peaks, indicating that thalamocortical relay cells (TCR) terminals act as the primary locus of astrocyte-driven compensation during

recovery. In contrast, adjustment in the strengthening rate of interneurons (IN), 'ω_{eSPin}' leads to comparatively smaller elevations in the recovered PR curve.

The main reason contributing to this result is as follows: *Firstly*. TCR neurons serve as the principal relay of sensory signals from thalamus to cortex [52], [53].Hence, boosting astrocyte activity at TCR synapses, 'ω_{eSPtcr}' directly strengthens the main information flow, which reflects in steeper PR. *Secondly,* TCR cells are excitatory in nature[37] and N-methyl-D-aspartate receptor (NMDA) receptor, which is the main receptor of glutamate [6] is a key player in excitatory transmission and synaptic transmission[2]. It is also well known from literature that long-term potentiation (LTP) of synaptic transmission depends on (NMDARs)[10]. Therefore, the above-mentioned facts contribute to the understanding that astrocyte-released glutamate at TCR synapses enhances NMDA receptor activation, facilitating to long-term potentiation therefore reflecting higher PR compared to the similar boost at IN terminals.

Table I depicts that increasing strengthening rate of indirect signaling at TCR enhances PR more effectively than at IN, highlighting the dominant role of excitatory terminals in recovery.

TABLE I
PR METRICS UNDER VARYING ASTROCYTIC STRENGTHENING RATES AT TCR AND IN

Parameter	Value	Peak PR
ω_{eSPtcr}	0.1	0.075
ω_{eSPtcr}	0.2	0.110
ω_{eSPtcr}	0.3	0.140
ω_{eSPin}	0.1	0.065
ω_{eSPin}	0.2	0.095
ω_{eSPin}	0.3	0.125

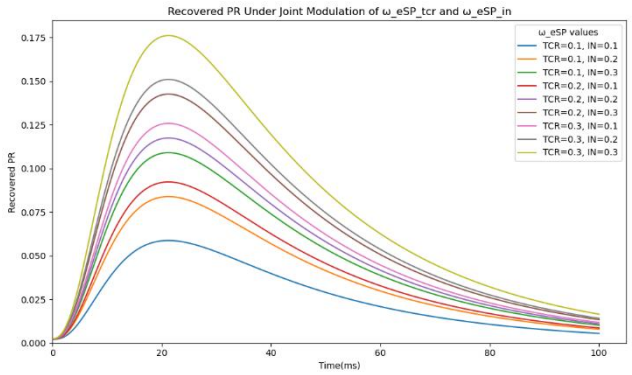

Fig.2. Recovery dynamics of TRN under combined effect of astrocytic strengthening rates at TCR and IN

Fig. 2 explores joint modulation of astrocytic strengthening rate at TCR and IN terminals. Curves with both parameters high (0.3, 0.3) show the highest PR peaks, revealing dual enhancement is critical. Partial modulation of either yields suboptimal recovery, emphasizing that astrocyte signaling must be coordinated across network nodes confirming the necessity of distributed glial control for global neuromodulation. For instance, increasing both from 0.1 to 0.3 significantly shifts the PR curve upward, forming a more pronounced effect. In contrast, enhancing only one parameter yields limited benefit, emphasizing the cooperative role of astrocyte signaling in distributed synaptic populations. This outcome aligns with biological insights, where astrocytic influence is known to operate via network-level compensation, especially in circuits affected by injury or neurodegeneration [45].

Role of astrocyte–synapse coupling weights of indirect signaling on PR recovery

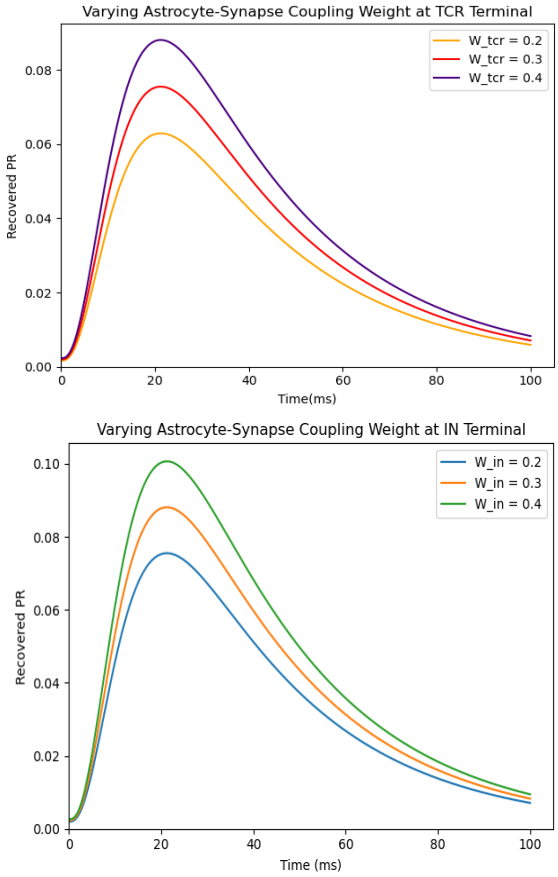

Fig.3. Recovery dynamics of TRN by varying astrocyte-synapse coupling weight of indirect signaling at TCR terminal (top)and IN terminal (bottom)

Fig. 3 demonstrates how the recovered PR evolves over time when the astrocyte–synapse coupling weights of indirect signaling i.e., 'W_{tcr}' for excitatory TCR terminal and 'W_{in}' for inhibitory IN terminal are varied.

It is clearly evident from Fig.3 that while increasing 'W_{tcr}' and 'W_{in}' from 0.2 to 0.4 does enhance PR but the rate and magnitude of improvement are lower in case of 'W_{tcr}' compared to 'W_{in}'. Hence, increasing 'W_{in}' can paradoxically enhance PR depicting the complex interplay between astrocytes and interneurons, which can be attributed to the following reason: literature [19] highlights a sophisticated role of astrocytes in neural circuits, demonstrating their active participation in synaptic plasticity by transforming inhibitory signals into excitatory ones through a specific molecular pathway involving $GABAB_B$ receptors, astrocytic calcium signaling, glutamate release, and mGluR activation. Previous

study [19] found that interneurons, which typically mediate inhibition, can activate calcium signaling in astrocytes, which specifically involves the activation of astrocytic $GABA_B$ receptors and when interneurons fire at high rates, they surprisingly potentiate excitatory synaptic transmission through these receptors. Hence, the ability of astrocytes to decode interneuron activity and transform inhibitory into excitatory signals contributes to the emergence of higher PR.

Table II clearly represents how PR improves with both 'W_{tcr}' and 'W_{in}', but the effect is more pronounced for 'W_{in}'.

TABLE II
PR METRICS UNDER VARIATION OF ASTROCYTE-SYNAPSE COUPLING WEIGHTS AT TCR AND IN

Parameter	Value	Peak PR
W_{tcr}	0.2	0.063
W_{tcr}	0.3	0.075
W_{tcr}	0.4	0.087
W_{in}	0.2	0.075
W_{in}	0.3	0.090
W_{in}	0.4	0.110

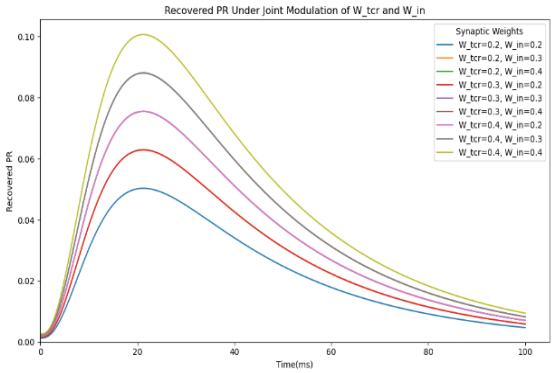

Fig.4. Recovery dynamics of TRN under combined effect of astrocyte-synapse coupling weight at TCR and IN

Fig. 4 demonstrates how the PR evolves over time when the astrocyte-synapse coupling weights of indirect signaling, 'W_{tcr}' and 'W_{in}' are varied in combination. It is clearly evident from the above figure that for low values of both 'W_{tcr}' and 'W_{in}' the PR curve remains subdued, indicating limited restoration of synaptic efficacy. As either 'W_{tcr}' or 'W_{in}' increases, the PR curve shows a noticeable elevation. The highest PR recovery is observed when both 'W_{tcr}' and 'W_{in}' are high, indicating a synergistic effect between astrocytic modulation of excitatory and inhibitory terminals. Lastly, it is important to note once again that despite both excitatory (TCR) and inhibitory (IN) weights being strong, IN dominates in contributing to PR recovery. This is an extremely interesting outcome contributing to therapeutic potential of visuomotor impairment in Alzheimer's Disease (AD).

These findings support the therapeutic potential and are consistent with the notion that astrocyte-neuron networks serve as intrinsic repair mechanisms in neurodegenerative disorders [46], [47]. This research study also emphasizes the modulatory power of astrocytic feedback and supports the concept that tuning astrocytic signaling parameters can be leveraged to control or optimize recovery in visuomotor impairment in AD. Therefore, in AD where ACh signaling is compromised/depleted, targeted enhancement of astrocytic signaling pathways may help stabilize disrupted circuits such as the TRN, which is critical for visuomotor impairment.

However, it is worth mentioning here that these sensitivity analyses reveal that the recovery level is strongly parameter-dependent across the explored parameter ranges. This parameter sensitivity underscores that the 70% recovery observed in the baseline configuration represents one validated scenario within a broader solution space. As demonstrated in Section VII of the main manuscript this computational prediction is supported by experimental observation of approximately 68% hemodynamic preservation, validating both the magnitude and mechanism of astrocytic compensation.

A.5 *Stability Analysis*

Fig.5 demonstrates that both healthy and recovered PR trajectories remain bounded within the physiologically valid interval [0, 1] throughout the extended simulation. No numerical divergence, negative values, or oscillatory artifacts are observed. The healthy state exhibits transient potentiation followed by gradual decay towards a stable plateau, while the recovered state also maintains similar PR trajectory. The damaged state remains at zero throughout, as expected.

This extended simulation confirms: (i) the explicit RK4 method with dt = 0.05 ms provides numerically stable integration for the timescales relevant to this study, (ii) observed temporal dynamics represent genuine model behavior rather than numerical instabilities, and (iii) the system exhibits well-behaved, bounded trajectories consistent with physiological constraints on release probability.

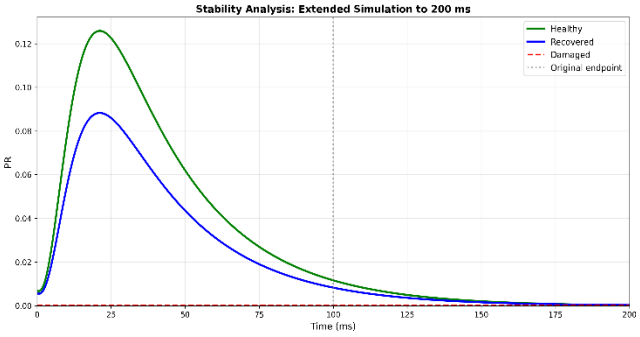

Fig. 5. Result of Stability Analysis: Extended Simulation

A.6 *Experimental Validation*

This section provides a comprehensive experimental validation of the computational model predicting astrocyte-mediated recovery of PR in TRN under cholinergic depletion in AD. Using a sequential pharmacological blockade design, the assessment of cognitive ability of 30 albino mice on a visuomotor integration task has been done by measuring the oxygen consumption from the recordings of functional near-infrared spectroscopy (fNIRS). Three conditions are examined:

(1) Healthy baseline, (2) Cholinergic blockade (scopolamine 0.3 mg/kg), and (3) Dual blockade (scopolamine + astrocyte inhibitor fluorocitrate 1 nmol ICV). The experimental design employs a within-subject sequential pharmacological blockade approach to isolate the contribution of astrocytes to synaptic recovery in thalamic circuits. By testing each mouse under three conditions, the astrocytic compensation mechanism predicted by the computational model is directly quantified.

Surgical Preparation and Recovery: Thirty albino mice (aged 8-12 weeks, weighing 22.4-28.2 g) are used. Twenty-four hours prior to the first experimental session, mice are anesthetized with an intraperitoneal injection of ketamine (100 µg/g) and xylazine (10 µg/g). After shaving the head and making a midline scalp incision to expose the skull, the periosteum over the skull surface is removed. A custom stainless-steel head plate is attached using cyanoacrylate glue and dental acrylic cement to enable head-fixed behavioral training.

Before each imaging session, a small craniotomy window (1 mm × 1 mm) is created over the motor cortex using a high-speed drill. The craniotomy is immediately covered with a glass coverslip to reduce brain motion, with one edge kept open to allow drug application when needed. Following surgery, all mice are allowed to recover for a minimum of 5 days before beginning the experiment. Mice are acclimated to the head-fixed imaging apparatus for approximately 10 minutes before each experimental session to reduce stress.

Training Protocol: After the recovery period, each mouse is trained on a head-fixed go/no-go visuomotor integration task in which they learned to make perceptual decisions based on visual cues. During training sessions, each mouse is positioned in a custom behavioral apparatus with the head plate secured to prevent movement while allowing comfortable posture.

The behavioral task followed a structured trial sequence with specific time frames. Each trial begins with an auditory cue that signaled the upcoming trial. Following the auditory cue, there is a 1-second delay period during which no stimulus is presented and the mouse is required to withhold licking. After this delay, a visual stimulus is presented for 2 seconds on a computer monitor positioned 15 cm from the mouse's right eye. The visual stimuli consisted of blue full-contrast set of horizontal gratings moving up and down, designated as the Target Stimulus A and red full-contrast set of vertical gratings moving right and left, designated as the Non-target Stimulus B.

Immediately following the 2-second stimulus presentation period, a retractable lick spout is rapidly extended to within reach of the mouse's tongue for a 1.5-second response epoch. During this response window, the mouse can choose to lick or withhold licking based on the stimulus identity. If the mouse licks in response to the Target Stimulus A, the response is scored as a "Hit" and if the mouse licks in response to the Non-target Stimulus B, the response is scored as a "False Alarm". If the mouse correctly withholds licking to the Non-target Stimulus B, the response is scored as a "Correct Reject". If the mouse fails to lick to the Target Stimulus A, the response is scored as a "Miss". After the 1.5 seconds response epoch, the lick spout is rapidly retracted and remains inaccessible during a 3-second inter-trial interval before the next trial began.

Training proceeded over 12-15 days for each mouse, with daily sessions consisting of 50-80 trials. Mice advance to experimental testing once they achieve stable performance criterion defined as d-prime greater than 1.5 for three consecutive sessions, indicating reliable discrimination between target and non-target stimuli.

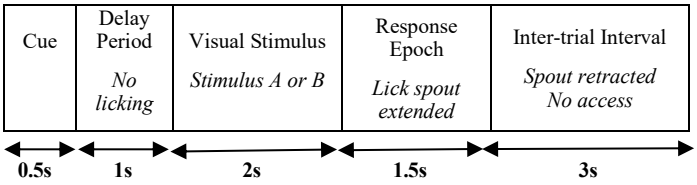

Fig. 6. Structure of stimulus

TABLE III
COMPLETE BEHAVIORAL LOGIC (DECISION MATRIX)

Stimulus Type	Mouse Action	Behavioral Outcome
Target A	Lick	Hit
Target A	No Lick	Miss
Non-Target B	Lick	False Alarm
Non-Target B	No Lick	Correct Reject

The fNIRS system installation and configuration: Following successful training, the fNIRS monitoring system is installed on each mouse. The whole-brain fNIRS device (NIRScoutTM, developed by NIRx Medical Technologies, LLC) is positioned over the skull with 8 infrared sources and 8 detectors (source-detector pairs referred to as optodes) operating at 7.81 Hz sampling rate. The fNIRS recordings obtained from the scalp of each mouse capture two primary blood concentration measurements: oxyhemoglobin (O_2Hb) and deoxyhemoglobin (HHb), both measured in mmol/L. Let $\Delta O_2Hb(t)$ and $\Delta HHb(t)$ denote the concentration changes in oxyhemoglobin and deoxyhemoglobin respectively at time instant 't' during an experimental trial. Since, $\Delta O_2Hb(t) > \Delta HHb(t)$, $\forall t$, the net oxygen consumption occurring in the cortical area above the LGN region of the mouse at any time instant 't' is given by equation (1) [50].

$$C = \Delta O_2Hb(t) - \Delta HHb(t) \quad (1)$$

Rationale for fNIRS measurement: The LGN functions as a first-order thalamic relay that transmits retinal information directly to the cortex and all information reaching the cerebral cortex pass through the thalamus [52]. Thus, alterations in TRN in LGN relay efficiency are expected to influence cortical activity. Moreover, it is well known that the TRN is a brain structure divided into a number of sections, and each section is concerned with performing a different function such as seeing, touching, hearing, and movement. Each of these sections is connected to the corresponding cortical area, which is associated with the regulation of sensory processing and formation of rhythmic activity in the thalamocortical system [8], [31]. Hence, changes in TRN-mediated modulation of LGN relay function whether degradation from cholinergic depletion or restoration through astrocytic compensation via functional TCR and IN are thus reflected in the hemodynamic activity of

the cortical area above the LGN. The cortical measurement is therefore used as a systems-level proxy for thalamic relay integrity.

Experimental Design: Each mouse is tested under three different pharmacological conditions using a within-subjects repeated-measures design. To prevent carryover effects between conditions, a minimum 48-hour washout period is implemented between successive experimental sessions, allowing complete drug clearance from the brain.

Experiment1: Healthy Baseline (Control)

For the first experimental session, each mouse receives a control injection of sterile saline solution. After a 15-minute waiting period to match the timing of subsequent drug conditions, the mouse is placed in the head-fixed behavioral apparatus with the fNIRS system actively recording. A 2-minute baseline recording is acquired before task onset. The mouse then performs 50-80 trials of the visuomotor integration task while fNIRS continuously records brain hemodynamic activity. Following task completion, an additional 2-minute post-task baseline is recorded. This session establishes the normal brain activity pattern for each mouse, providing the reference baseline (100%) for subsequent comparisons.

Experiment 2: ACh Blockade (Cholinergic Depletion)

For the second experimental session (conducted 48 hours after the first session), each mouse receives an intraperitoneal injection of scopolamine hydrobromide (0.03 mg/kg body weight dissolved in sterile saline). Scopolamine is a muscarinic acetylcholine receptor antagonist that blocks cholinergic neurotransmission in the brain, mimicking the cholinergic deficit observed in AD [22]. After a 15-minute waiting period to allow the drug to reach peak brain concentration and achieve central receptor blockade, the mouse is placed in the behavioral apparatus. The identical recording protocol is followed: 2-minute pre-task baseline, 50-80 task trials with continuous fNIRS recording, and 2-minute post-task baseline. This session tests the hypothesis that astrocytes would provide compensatory support to maintain brain function despite loss of cholinergic signaling. The percentage of brain activity preserved under this condition reveals the magnitude of astrocytic compensation.

Experiment3: Dual Blockade (Cholinergic and Astrocytic Inhibition)

For the third experimental session (conducted 48 hours after the second session), each mouse receives dual pharmacological blockade. First, scopolamine hydrobromide (0.03 mg/kg) is administered intraperitoneally. Then, 15 minutes later, fluorocitrate (FC) (5 µM diluted with artificial cerebrospinal fluid (ACSF) solution) is applied topically onto the motor cortex through the open edge of the cranial window. Following an additional 15-minute waiting period (30 minutes total from FC application), the mouse is placed in the behavioral apparatus and the identical recording protocol is executed. The Tricarboxylic acid (TCA) cycle is inhibited by FC by targeting aconitase, disrupting carbon flux, and impairing adenosine triphosphate (ATP) production. According to literature, FC temporarily inhibits the aconitase activity in the glial cells, thereby leading to citrate accumulation in the TCA cycle and ultimately causing obstruction in glutamine synthesis. FC also blocks astrocytic functions such as ATP production and calcium signaling [21]. This session is critical for establishing the causal role of astrocytes: if astrocytes are responsible for the preservation observed in experiment 2, then blocking astrocytic function in experiment 3 shall cause brain activity to collapse to a much lower level.

Results and Analysis: Table IV presents the comprehensive dataset from all 30 mice across three experimental conditions. Complete data from all three conditions are obtained from N=22 mice (73.3%). Attrition occurred due to mortality in the ACh Block condition (M08, M20; N=2, 6.7%) and Dual Block condition (M04, M09, M13, M16, M23, M28; N=6, 20%). Oxygen consumption values are peak amplitudes during task performance relative to pre-stimulus baseline. "%ACh blocked" and "%Dual blocked" columns show preservation relative to Healthy baseline. Status indicates whether complete data are obtained across all three conditions.

TABLE IV
INDIVIDUAL MOUSE DATA SUMMARY

Mouse ID	Sex	Weight (g)	Oxygen consumption (Healthy) (mmol/L)	Oxygen consumption (ACh blocked) (mmol/L)	% ACh blocked	Oxygen consumption (Dual blocked) (mmol/L)	% Dual blocked	Status
M01	M	25.0	2.534	1.662	65.6	0.074	2.9	Complete
M02	F	26.0	2.469	1.741	69.7	0.058	2.3	Complete
M03	M	24.0	2.134	1.458	68.3	0.060	2.8	Complete
M04	F	24.6	2.475	1.603	64.8	-	-	Died Dual
M05	M	25.3	2.393	1.594	66.6	0.036	1.5	Complete
M06	F	24.3	2.410	1.712	71.1	0.038	1.6	Complete
M07	M	26.8	2.392	1.505	62.9	0.059	2.5	Complete
M08	F	24.6	2.172	-	-	-	-	Died ACh
M09	M	24.1	2.656	1.777	66.9	-	-	Died Dual
M10	F	23.7	2.491	1.751	70.3	0.094	3.8	Complete
M11	M	27.9	2.505	1.654	66.0	0.072	2.9	Complete
M12	F	23.5	2.469	1.640	66.4	0.075	3.0	Complete
M13	M	25.1	2.091	1.413	67.6	-	-	Died Dual
M14	F	22.4	2.569	1.817	70.7	0.092	3.6	Complete
M15	M	26.7	2.469	1.642	66.5	0.057	2.3	Complete
M16	F	25.4	2.365	1.582	66.9	-	-	Died Dual
M17	M	24.8	2.696	1.803	66.9	0.087	3.2	Complete
M18	F	25.1	2.310	1.667	72.2	0.055	2.4	Complete
M19	M	28.2	2.348	1.693	72.1	0.038	1.6	Complete
M20	F	25.9	2.600	-	-	-	-	Died ACh
M21	M	26.7	2.545	1.775	69.8	0.069	2.7	Complete
M22	F	23.7	2.523	1.729	68.5	0.088	3.5	Complete
M23	M	27.1	2.286	1.583	69.2	-	-	Died Dual
M24	F	23.7	2.426	1.716	70.7	0.080	3.3	Complete
M25	M	26.3	2.517	1.659	65.9	0.076	3.0	Complete
M26	F	25.1	2.306	1.617	70.1	0.104	4.5	Complete
M27	M	28.1	2.402	1.568	65.3	0.080	3.3	Complete
M28	F	25.0	2.391	1.590	66.5	-	-	Died Dual
M29	M	25.2	2.440	1.697	69.6	0.093	3.8	Complete
M30	F	25.2	2.800	1.818	64.9	0.127	4.5	Complete

Calculation of Key Outcome Measures: For each mouse and each condition, trial-averaged oxygen consumption amplitudes are calculated by averaging across all correct trials (Hits and Correct Rejects) within that session, excluding error trials (False Alarms and Misses) and this yielded three values per mouse: mean oxygen consumption amplitude for healthy baseline, mean oxygen consumption amplitude for ACh blockade, and mean oxygen consumption amplitude for dual blockade. Group-level statistics are then computed by averaging across all mice that successfully completed each condition, with standard error of the mean (SEM) calculated to quantify inter-animal variability.

The primary outcome measures calculated to test the central hypotheses are given below:

Preservation Ratio Under ACh Blockade: For each mouse, the ACh preservation ratio is calculated as *(Oxygen consumption (under ACh blocked) / Oxygen consumption (under Healthy baseline)) × 100%,* representing the percentage of normal brain activity that remains when only AChis blocked. This value quantifies the compensatory mechanisms mediated by astrocytes during the cholinergic loss. Group mean ACh preservation is computed by averaging individual mouse ratios.

Preservation Ratio Under Dual Blockade: Similarly, the Dual preservation ratio is calculated as *(Oxygen consumption (under Dual blocked) / Oxygen consumption (under Healthy baseline)) × 100%*, representing the percentage of normal brain activity remaining when both ACh and astrocytic function are blocked. This value quantifies only the residual neuronal function without any astrocytic compensation.

In Fig.7 each colored line represents one mouse's hemodynamic response trajectory across conditions (N=22 completed all three conditions), while the bold black line with diamond markers indicates the group mean. The tight clustering of individual trajectories demonstrates the robustness of the astrocytic compensation phenomenon across animals.

Group Mean Performance Across Conditions: Table V presents the group-level statistics that form the basis of model validation. Values represent mean ± SEM for all mice that completed each condition.

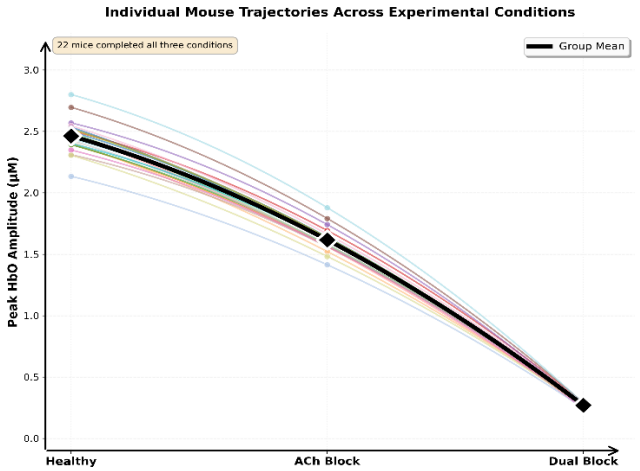

Fig. 7. Individual mouse hemodynamic response trajectories across experimental conditions

TABLE V
GROUP HEMODYNAMIC RESPONSES ACROSS EXPERIMENTAL CONDITIONS

Condition	N	Mean Oxygen consumption (mmol/L)	SD (mmol/L)	SEM (mmol/L)	% of Healthy
Healthy Baseline	30	2.44	0.155	0.028	100
ACh Blockade	28	1.66	0.103	0.019	68
Dual Blockade	22	0.07	0.022	0.005	3

TABLE VI
BEHAVIORAL RESPONSE AND NEURAL ACTIVITY ACROSS EXPERIMENTAL CONDITIONS

Cases	Behavioral Response	Neural Activity (Oxygen consumption at cortical area above LGN) (mmol/L)
Healthy Baseline	Frequent repeated licking	2.44±0.028
ACh Blockade	Infrequent non-repeated licking	1.66±0.019
Dual Blockade	No licking	0.07±0.005

Temporal Dynamics of Hemodynamic Responses: Hemodynamic response analysis confirms the computational model's temporal predictions. All three conditions—healthy (2.44 mmol/L), ACh blockade (1.66 mmol/L), and dual blockade (0.07mmol/L)—peak at 2.3 seconds post-stimulus, demonstrating that astrocytic compensation preserves both the amplitude (68% under ACh blockade) and the temporal fidelity of neural responses at the cortical recording site above the LGN.

Under ACh blockade, despite 68% amplitude preservation, the peak timing remains at 2.3 s, showing that astrocytic glutamate release restores release probability without altering response kinetics. Under dual blockade, the severely reduced amplitude (0.07 mmol/L, 3% of baseline) also maintains the 2.3s peak timing as demonstrated in Fig.8. This temporal consistency across all conditions validates that astrocytic feedback mechanisms operate on timescales compatible with normal neural processing and preserve both the magnitude and temporal structure of thalamocortical relay function.

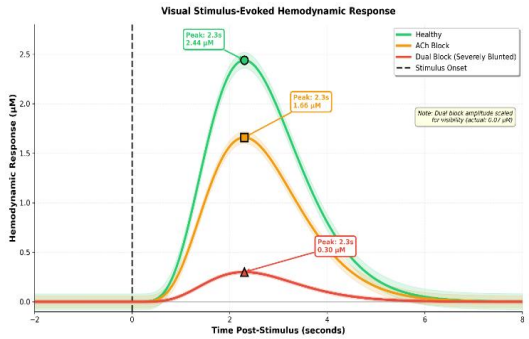

Fig. 8. Temporal dynamics of visual stimulus-evoked hemodynamic responses

TABLE VII
MODEL VS EXPERIMENTAL COMPARISON

Condition	N	Model Prediction	Experimental Result
Healthy Baseline	30	100%	100%
ACh Blockade	28	70%	68%
Dual Blockade	22	~0%	3%

The experimental results provide evidence for three critical aspects of the computational model:

Mechanistic accuracy: The model correctly captures the biological mechanism by which astrocytes compensate for cholinergic loss. Astrocytic feedback from TCR and IN restores synaptic transmission probability in the thalamocortical circuit, as predicted.

Quantitative precision: The model's predicted PR restoration to ~70% is in close agreement with the experimental hemodynamic preservation of 68% within 2% error, demonstrating that the model's parameter values accurately represent the biological system.

Causal validation: The dual blockade experiment causally confirms that the preserved activity is specifically attributable to astrocytes. Eliminating astrocytic function removes the compensation and reveals the underlying low baseline activity (~0%) predicted by the model when only residual neuronal function remains.

Our experimental results therefore, demonstrate significant astrocytic compensation in maintaining thalamic neural activity following cholinergic impairment. Moreover, temporal analysis of hemodynamic responses provides additional validation of the computational model. All experimental conditions exhibit identical peak timing at 2.3 seconds following stimulus onset, confirming the model's prediction that astrocytic compensation operates through mechanisms that preserve normal temporal dynamics. These findings quantitatively establish that astrocytes provide critical functional rescue following cholinergic loss, supporting their therapeutic potential in AD and other cholinergic deficit disorders.